Effect of Solution Chemistry on Schwertmannite Formation

Hannah Elizabeth King

Thesis submitted to the faculty of the Virginia Polytechnic Institute and State University
in partial fulfillment of the requirements for the degree of

Master of Science
In
Geosciences

Frederick M. Michel, Chair
Michael F. Hochella
J. Donald Rimstidt

June 30, 2015
Blacksburg, VA

Keywords: schwertmannite, goethite, crystallinity, solution chemistry, thermal analysis, wet chemical analysis, electron microscopy

Effect of Solution Chemistry on Schwertmannite Formation

Hannah E. King

ABSTRACT

Natural nanominerals are abundant in Earth's critical zone and important in innumerable environmental processes that affect water quality. The chemical behavior of many natural nanominerals is related to their extreme small size (<10 nm) and high surface area. Atomic structural and chemical heterogeneity are also important factors affecting nanoparticle reactivity, and are a consequence of the mechanisms and complex (natural) conditions by which they form. The relationships between these factors remain poorly understood and limit our ability to predict the formation, transformation, and chemical behavior of natural nanominerals in the environment.

We are using a poorly crystalline ferric hydroxysulfate nanomineral, schwertmannite, as a model system to understand the effect of formation conditions, specifically solution chemistry, on its physico-chemical characteristics. Previous studies indicate schwertmannite has highly variable bulk sulfate (Fe/S molar from 3-15) and water contents (Caraballo et al., 2013). In addition, both natural and synthetic schwertmannites have recently been described as "polyphasic" (i.e., consisting of sulfate-poor, goethite-like ordered domains embedded in a sulfate-rich, amorphous material) from observations using transmission electron microscopy (French et al., 2012). We hypothesize that solution chemistry at the time of schwertmannite formation directly affect its composition and structure.

Using a factorial experiment design, we investigated the effects of increasing solution sulfate concentration ($[SO_4]/[Fe]$ at 1, 2, 3 and 5) and pH (2.4-5.6) on the crystallinity and composition of the products. Ferric hydroxide and hydroxysulfate solids were precipitated in batches by the rapid oxidation of Fe(II) by hydrogen peroxide, similar to what is seen in natural environmental systems. Sulfate and hydroxide concentrations were varied by addition of $NaSO_4$ and NaOH, respectively. Solids were characterized using synchrotron X-ray diffraction (XRD), thermogravimetric analysis (TGA), differential scanning calorimetry (DSC), inductively coupled plasma-mass spectrometry (ICP-MS), scanning electron microscopy (SEM), and high resolution-transmission electron microscopy (HR-TEM). Our results show that schwertmannite is the only precipitate formed at low pH and that goethite rapidly becomes dominant at pH > 3.5. High-resolution TEM showed our synthetic schwertmannite samples consist of poorly crystalline goethite-like nanodomains within an amorphous solid, similarly seen in previous results. ICP-MS results reveal a narrow Fe/S molar ratio of 4.5 ±0.1 for our synthetic schwertmannite, which suggests that schwertmannite chemical composition does not depend strongly on pH or initial solution sulfate concentration. Increasing pH from 2.4 to 3.2 also has little effect on the crystallinity, bulk Fe/S ratio and water contents of schwertmannite. Increasing solution $[SO_4]/[Fe]$ also has little to no impact on crystallinity, water content or the amount of sulfate incorporated in schwertmannite. Thus, schwertmannite crystallinity and composition is not affected by initial solution sulfate and concentration under our experimental conditions.

Thermal analysis allows us to independently measure OH and SO_4 content in synthetic schwertmannite. In doing so, we propose a more accurate chemical formula ($Fe_8O_z(OH)_{24-2z-2x}(SO_4)_x$). The average stoichiometry based on thermal analysis of schwertmannite precipitated at $[SO_4]/[Fe]$ = 1 and pH ranging from ~2.4 – 2.9 is $Fe_8O_{6.51}(OH)_{8.4}(SO_4)_{1.28}$. Interestingly, the calculated number of moles of oxygen is less than 8, which suggests that the standard formula $Fe_8O_8(OH)_{8-2x}(SO_4)_x$ is incorrect. These results for synthetic samples provide important constraints for future studies aimed at better understanding the formation, compositional variability and chemical behavior of natural schwertmannite.

ACKNOWLEDGEMENTS

Without a doubt my advisor, Dr. Marc Michel, has exceeded every expectation as a mentor I could have hoped for. Before I even began graduate school at Virginia Tech, his enthusiasm and passion towards nanoscience made it clear he would be the perfect person to learn from over the course of two years. Marc's wisdom, guidance and patience led to the completion of this thesis project that I am so proud of. But more than that, Marc taught me life skills that I will take with me wherever I travel to. Thank you to my other committee members, Mike and Don for the scientific discussions and encouragement. Within our Environmental Nanoscience group, Sarah Ulrich and Rui Serra Maia provided different attributions that allowed me to become a better scientist. However, their friendship while at Virginia Tech is something I will forever be grateful for.

Over the course of my thesis I used a range of characterization techniques that required multiple training sessions. While learning and becoming familiar with each technique, this took time away from the busy lives of many individuals. I would like to thank Dr. Neil Johnson for his time teaching me how to use the XRD, Hesham Elmkharram and Dr. Tom Staley for guidance with thermal analysis, Athena Tilley for analyzing all my ICP-MS samples, and Dr. Chris Winkler for his time taking beautiful TEM images. Without these professionals, I would not have the results that led to the completion of this work.

Finally, thank you for the continuous support and love from my family and friends. Without you, I wouldn't have the passion and curiosity for science and life that I possess today. The impact you have made and will continue to have on me is endless.

TABLE OF CONTENTS

LIST OF FIGURES

LIST OF TABLES

1. INTRODUCTION

The precipitation of secondary Fe(III) minerals from acid mine drainage (AMD) is an important process due to its effect on biogeochemical cycling of metals and other pollutants. AMD is generated when mining activities expose pyrite (and other sulfide minerals) to water and air, and biotic and abiotic processes oxidize the pyrite to produce SO_4^{2-}, Fe^{2+} and H^+ in solution. The overall weathering of pyrite is described by equation (1)

$$FeS_{2\,(aq)} + 3.75\ O_{2\,(g)} + 3.5\ H_2O_{\,(l)} = Fe\,(OH)_{3\,(s)} + 2H_2SO_{4(aq)} \qquad (1)$$

Pyrite decomposition is actually a complex biogeochemical process involving hydration, hydrolysis, and oxidation reactions, as well as microbial catalysis (Nordstrom and Alpers, 1999). Fe(II) oxidation and the precipitation of $Fe(OH)_3$ solids (right side of eq. 1) is also complicated, as it is known to depend on various geochemical parameters such as pH and SO_4^{2-} concentration. Jarosite can form at low pH (<3) and high sulfate concentrations. As pH increases, schwertmannite, ferrihydrite, goethite and lepidocrocite are known to precipitate. Due to rapid precipitation kinetics and varying geochemical conditions, these phases frequently occur as mixtures commonly referred to as ochre or "yellow boy" in AMD (Jonsson et al., 2005, Bigham and Nordstrom (2000)).

Minerals such as goethite, ferrihydrite and schwertmannite are of broad interest at many of AMD sites because they exhibit high surface area and an affinity for arsenic, selenium, and chromium. The high chemical reactivity of these solids is related in part to their extreme small (nanometer) particle size and complex atomic structures. However, despite decades of research on both natural and synthetic samples, the exact formation mechanisms of these different minerals, as well as their exact chemical and mineralogical properties remain largely unknown (Bigham and Nordstrom, 2000).

First found in nature by Brady et al. (1986) and considered an "amorphous" ferric hydroxide, schwertmannite was later characterized by Bigham et al. (1990) and given the proposed chemical formula of $Fe_8O_8(OH)_{8-2x}(SO_4)_{X;}$ ($1<x<1.75$). Schwertmannite was officially accepted as a mineral in 1994 based off of samples from an acid coal mine drainage in Ohio, U.S.A, and later from Pyhä salmi, Finland (Bigham et al., 1994). Defining the properties of

schwertmannite is challenging because it is poorly crystalline, metastable, and commonly admixed with other nanophase Fe minerals (Murad et al., 1994).

The crystal structure of schwertmannite remains highly debated. Originally, schwertmannite's particles were described as fine needles forming rounded aggregates 200 to 500 nm in diameter and exhibiting a unique "pin-cushion" or "hedge-hog" morphology (Bigham and Nordstrom, 2000). Bigham et al. (1994) suggests schwertmannite has an akaganéite-type ($Fe_8O_8(OH,Cl)_8$) structure with SO_4 in the tunnels rather than Cl. More recently, schwertmannite has been described as a polyphasic nanomineral that exhibits a nanoscale structural heterogeneity and consists of nanocrystalline areas between three to five nanometers in diameter showing goethite-like domains embedded in a sulfate-rich amorphous matrix (French et al., 2012, 2014). In the study by Hockridge et al. (2009), observations from HR-TEM agreed with French et al. stating nanocrystalline domains have a goethite-like structure. In comparison, Fernandez-Martinez et al. (2010) interprets schwertmannite being more similar to Bigham et al. (1990) whereas Loan et al. (2004) concludes schwertmannite's structure is more ferrihydrite-like.

Along with nanoscale structural heterogeneity, schwertmannite has a variable chemistry with the Fe:S molar ratio ranging from 3.77 to 15.53 (Caraballo et al., 2013). The variable OH^- and SO_4^{2-} content suggest that schwertmannite's chemical composition might vary as a function of conditions at the time of formation. Yu et al. (2002) reported schwertmannite has little to no structural OH based on thermogravimetric analysis and therefore its chemical formula should actually be $Fe_2O_{3-x}(SO_4)x\cdot nH_2O$. If OH is assumed to be a fundamental part of schwertmannite's formula, then according to equation (2) from Bigham et al. (1994), changes for *x* in SO_4^{2-} concentration is compensated by an 8-2x change in OH^- concentration, where *x* values in nature typically range from 0.5 to 2 (Caraballo et al., 2013).

$$Fe_8O_8(OH)_{8-2x}(SO_4)_X + (24-2x)\,H^+ = 8Fe^{3+} + xSO4^{2-} + (16-2x)H_2O \qquad (2)$$

In the past, variation in S content has been attributed to different amounts of SO_4^{2-} absorbed to the mineral surface and within the bulk structure (Loan et al., 2004, Caraballo et al., 2013). Currently, there is no clear answer as to why schwertmannite has such a variable chemistry.

THESIS OVERVIEW

This Master's thesis examines how the crystallinity and composition of the synthetic ferric (oxyhydr)oxide hydroxysulfate, schwertmannite, depends on the initial solution conditions under which it forms. Previous studies suggested that schwertmannite (nominally $Fe_8O_8(OH)_{8-2x}(SO_4)_x$, where $1 < x < 2$) has a highly variable sulfate content with Fe/S molar ratios ranging from 3-15 (see Caraballo et al., 2013 for review), but it remains unclear what factors control sulfate uptake during schwertmannite formation. It is also unclear how varying sulfate content impacts schwertmannite crystallinity, which prior research suggests is a heterogeneous mixture of partially nanocrystalline and amorphous solids. Addressing these uncertainties will improve our understanding of schwertmannite formation in nature and will have significant implications for understanding its role in biogeochemical cycling of metals in contaminated environments impacted by acid mine drainage.

The overarching hypothesis of this project is that initial solution chemistry, specifically SO_4:Fe molar ratio and pH determine the crystallinity and composition of schwertmannite. The specific hypotheses tested in this study include:

1. Increasing solution pH will favor the formation of an FeOOH-like component in schwertmannite, thus resulting in higher crystallinity, increased water content, and decreased sulfate content.

2. Increasing initial solution sulfate concentration (i.e., SO_4:Fe molar ratio) will suppress the formation of FeOOH, thus resulting in schwertmannite with lower crystallinity (more sulfate-rich amorphous content), decreased water content, and increased sulfate content.

We used systematically varied synthesis conditions and the systematic application of complementary analytical characterization methods to examine to what extent varying initial solution chemistry affected the composition and crystallinity of the products. A total of 36 solids were precipitated in individual batches at SO_4:Fe ratios of 1, 2, 3 and 5 (72-360 mM) and pH ranging from ~2.4 - 5.6. Average [SO_4] concentrations found in nature range from ~208-1100 mM in the Richmond Mine at Iron Mountain, CA (Nordstrom et al., 2000) to sulfate concentrations as low as ~0.96 in Elizabeth and Ely mine sites in central Vermont (Hammarstrom et al. (2005). Average pH ranges from 2-4 in acid mine waters (Nordstrom and Alpers, 1999). Thus, the SO_4:Fe ratios in the synthetic solids at 3 and 5 are comparable to

average [SO_4] concentrations in nature. Synthesis pH is also within the same pH range typically found in natural acid mine drainages. Mineralogical characterization was performed using X-ray diffraction (XRD), thermogravimetric (TG) analysis, differential scanning calorimetry (DSC), inductively coupled plasma - mass spectrometry (ICP-MS), scanning electron microscopy (SEM), and high-resolution transmission electron microscopy (HR-TEM).

This thesis is divided into the following chapters: Introduction, Methods, Results, Discussion, Conclusions and Future Studies, and an Appendix. Chapter 1 introduces the project and provides background information pertinent to the main questions addressed by this research. Chapter 2 provides information on the analytical characterization methods used and Chapter 3 gives the results. The discussion of our results (Chapter 4) is broken into 4 parts that address: 1) justification of synthesis strategy, 2) effects of initial solution sulfate [SO_4] and pH on the bulk mineralogy of the entire sample series, 3) effects of initial solution [SO_4] and pH on the bulk and nanoscale structure and composition of schwertmannite, and 4) implications of the results in terms of schwertmannite stoichiometry and chemical formula. Chapter 5 summarizes the conclusions of this work and also identifies new ideas and directions for future related studies. The appendices provide supporting data and figures related to this study.

2. MATERIALS AND METHODS

2.1 Ferric (oxy)hydroxide and hydroxysulfate synthesis

Ferric (oxy)hydroxides and hydroxysulfate solids were synthesized at room temperature using a method adapted from Regenspurg et al. (2004). All chemicals were reagent grade and used as received without additional purification. A 0.072 M ferric sulfate solution was prepared dissolving 4.8 g $FeSO_4 \bullet 7H_2O$ (Amresco) into 240.0 mL of deionized water (DI). An appropriate amount of Na_2SO_4 (Sigma-Aldrich) was dissolved in the iron sulfate solution for syntheses at higher SO_4:Fe ratios of 2, 3 and 5. Four hundred µL of H_2O_2 (30% wt/wt, Sigma-Aldrich) was mixed with 80.0 mL of deionized water to produce a total H_2O_2 concentration of 0.15% wt/wt. $NaHCO_3$ (Sigma-Aldrich) was dissolved in the diluted H_2O_2 solutions for syntheses at higher pH. Ferrous iron oxidation was initiated by rapidly mixing the diluted H_2O_2 solution, in some cases also containing dissolved $NaHCO_3$, with the ferrous sulfate solutions under vigorous stirring. The precipitates and solutions were stirred continuously for 75 minutes, followed by a period of aging at static fluid conditions (no stirring) that ranged from 22 - 24 h. The "initial"

and “final” pH was measured and recorded immediately after stirring ended at 75 minutes and at the end of aging at static fluid conditions, respectively. pH and other information related to each sample synthesis are included in **Table 2.1**. Immediately after aging, the supernatant was decanted and the wet solids (approximately 0.5 - 1 g per synthesis) were transferred to a 50 mL plastic centrifuge tube. The solids were repeatedly centrifuged (10,000 rpm for 10 minutes), decanted, and rinsed with deionized water to remove residual electrolytes. The resulting wet pastes were recovered and dried at room temperature. The dry powders were gently ground by mortar and pestle, loaded and capped in 2 mL plastic tubes and stored in a desiccator. The color of the powders ranged from dullish yellow to deep red/brown at low pH and high pH, respectively. Samples are identified according to the SO_4:Fe ratio (**Table 2.1**) and the sample number, which increases with pH. For example, “R1(S1)” was synthesized at SO_4:Fe=1 and at the lowest pH (i.e., no $NaHCO_3$ added) and“R5(S9) was synthesized at SO_4:Fe=5 and at the highest pH (i.e., maximum amount of $NaHCO_3$ added).

2.2 Wet chemical analyses

The chemical composition of each sample was determined using inductively coupled plasma mass spectrometry (ICP-MS). Approximately 0.02 g of each sample was dissolved in 1 mL hydrochloric acid (HCl) (36% wt/wt) and 9 mL DI water. ICP-MS analyses were performed at the Virginia Tech Soil Testing Laboratory using a Spectro Analytical instrument to determine total concentrations (mg L^{-1}) of iron, sulfur, calcium, and sodium.

2.3 Laboratory X-ray diffraction Analysis

X-ray diffraction (XRD) data were collected using a Rigaku MiniFlex II Desktop X-ray diffractometer equipped with a CuKα source (30 kV to 15 mA). Air dried solids were ground using an agate mortar and the powders were mounted on silicon zero background sample holders. Diffracted intensities from the samples were collected from 15 to 80° 2θ in 0.2° increments. Exposure time was 10 seconds per step and the sample holder was rotated continuously during data collection. Laboratory XRD data (not shown) were used primarily for initial screening of mineralogy and assessing sample quality, such as the effectiveness of rinsing and centrifugation to remove residual salts. Details of structural characterization by synchrotron XRD are given below.

2.4 Synchrotron X-ray diffraction Analysis

Synchrotron X-ray diffraction data of the dry powders loaded in 1 mm O.D. Kapton capillaries were collected at beamline 11-ID-B [~58.6 keV, λ = 0.2114 Å] of the Advanced Photon Source, Argonne National Laboratory (APS-ANL, Argonne, IL). An amorphous Si area detector system (Perkin Elmer) was used for data collection. A CeO_2 standard (NIST diffraction intensity standard set 674a) was used to calibrate the sample-detector distance and nonorthogonality of the detector relative to the incident beam. Conversion of data from 2D to 1D was performed using Fit2D (Hammersley et al. 1996; Hammersley, 1998). The background intensity measured for a blank (empty) capillary was subtracted from each sample using Excel.

2.5 Thermal Analysis

Thermogravimetric (TG) and differential scanning calorimetry (DSC) analyses of the dry powdered samples were conducted at the Virginia Tech Thermal Properties and Polymers Lab using a Netszch STA TGA/DSC. In each run, 10-20 mg of solid was heated at a rate of 10 ºC min^{-1} from ~20 to 800 ºC under N_2 gas.

Selected samples were pre-heated for 24 h at 115 °C in a Thermo Scientific Thermolyne oven prior to thermal analysis. The samples were cooled inside the oven for ~5 minutes prior to loading into the TG-DSC.

2.6 Electron Microscopy Analysis

Scanning electron microscopy (SEM) images of selected samples R1(S1, S3, S7 and S9) were recorded on a LEO (Zeiss) 1550 field-emission SEM operating at 5 keV, at the Nanoscale Characterization and Fabrication Laboratory (NCFL) in the Institute for Critical Technology and Applied Science (ICTAS) at Virginia Tech. A small amount of powder was dispersed in ~0.5 mL of ethanol and sonicated for 2 minutes. Then a drop of suspension was placed onto a silicon wafer adhered to an aluminum SEM stubs using copper tape.

High-resolution transmission electron microscopy (HR-TEM) imaging was performed on a JEOL 2100 operating at 200 keV (NCFL, ICTAS, Virginia Tech). Samples were suspended in ethanol and placed in a sonicating bath for 2 minutes to disperse aggregates as described by French et al. (2014). A droplet of sample was placed on a gold TEM grid with lacey carbon

support film and wicked dry with a Kimwipe. A selected area electron diffraction (SAED) pattern was obtained for only R1(S9) and was collected from an area consisting of particle aggregates. Analyses by fast Fourier transform (FFT) measured d-spacings from selected areas of the images was done using *Digital Micrograph* (Gatan Inc.).

Table 2.1. Overview of synthesis conditions. Each synthesis solution consisted of 80 mL of the H_2O_2/bicarbonate solutions mixed with 240 mL of ferrous sulfate solution. Fe^{2+} concentration was 72 mM in all syntheses. The first entry in each cell is the sample identifier.

[$NaHCO_3$] in mM	"R1" SO_4:Fe = 1 [SO_4] = 72 mM	"R2" SO_4:Fe = 2 [SO_4] = 144mM	"R3" SO_4:Fe = 3 [SO_4] = 216 mM	"R5" SO_4:Fe = 5 [SO_4] = 360 mM
0.0	R1(S1)	R2(S1)	R3(S1)	R5(S1)
29.8	R1(S2)	R2(S2)	R3(S2)	R5(S2)
59.5	R1(S3)	R2(S3)	R3(S3)	R5(S3)
89.3	R1(S4)	R2(S4)	R3(S4)	R5(S4)
119.0	R1(S5)	R2(S5)	R3(S5)	R5(S5)
148.8	R1(S6)	R2(S6)	R3(S6)	R5(S6)
178.6	R1(S7)	R2(S7)	R3(S7)	R5(S7)
208.3	R1(S8)	R2(S8)	R3(S8)	R5(S8)
238.1	R1(S9)	R2(S9)	R3(S9)	R5(S9)

3. RESULTS

3.1 Composition - Wet Chemical and Thermal Analyses

Four series of ferric oxyhydroxide sulfate samples (9 samples per series, 36 total, see table 2.1) were synthesized at different initial sulfate to iron (SO_4:Fe) ratios of 1, 2, 3 and 5 and at varied pH ranging from ~2.4 to ~5.8. SO_4:Fe molar ratios in the starting solution and final solids (as analyzed by ICP-MS) and pH values recorded at the end of each synthesis are listed in **Table 3.1**.

Table 3.1 ICP-MS results for 36 ferric oxyhydroxide sulfate samples. The first column is the sample identifier. The second and third columns are the initial and final pHs, respectively. The last four columns are total Ca, Na, S and Fe (mg/L) measured by ICP-MS.

Sample ID	Initial	Final	Ca ($mg\ L^{-1}$)	Na ($mg\ L^{-1}$)	S ($mg\ L^{-1}$)	Fe ($mg\ L^{-1}$)
R1(S1)	2.46	2.44	<0.006	0.614	120	968
R1(S2)	2.53	2.51	<0.006	0.549	135	1041
R1(S3)	2.61	2.58	<0.006	0.547	120	926
R1(S4)	2.72	2.69	<0.006	0.723	185	1429
R1(S5)	2.92	2.90	<0.006	0.622	138	1122
R1(S6)	3.57	3.38	<0.006	0.671	139	1195
R1(S7)	4.61	3.95	<0.006	0.037	9.84	152
R1(S8)	5.12	4.78	<0.006	0.018	3.35	151
R1(S9)	5.72	5.62	<0.006	0.026	3.00	177
R2(S1)	2.59	2.57	<0.006	0.543	110	888
R2(S2)	2.63	2.60	<0.006	0.541	110	866
R2(S3)	2.70	2.71	<0.006	0.522	108	845
R2(S4)	2.82	2.82	<0.006	1.44	140	1074
R2(S5)	2.94	2.94	<0.006	0.690	94.9	764
R2(S6)	3.39	3.28	<0.006	0.752	115	1046
R2(S7)	4.53	4.09	<0.006	0.019	17.6	299
R2(S8)	5.10	4.76	<0.006	0.044	7.17	326
R2(S9)	5.64	5.40	<0.006	0.029	3.84	237
R3(S1)	2.65	2.64	<0.006	0.728	100	830
R3(S2)	2.71	2.72	<0.006	0.664	95.4	753
R3(S3)	2.77	2.79	<0.006	0.963	106	827
R3(S4)	2.88	2.87	<0.006	0.879	100	779
R3(S5)	3.11	3.08	<0.006	3.42	111	863
R3(S6)	3.76	3.61	<0.006	1.58	77.3	670
R3(S7)	4.72	4.22	<0.006	0.145	15.1	225
R3(S8)	5.46	5.28	<0.006	0.061	3.90	126
R3(S9)	5.82	5.73	<0.006	0.096	3.71	206
R5(S1)	2.75	2.76	<0.006	0.618	585	71.9
R5(S2)	2.81	2.82	<0.006	0.734	466	58.5
R5(S3)	2.88	2.90	<0.006	0.636	805	102
R5(S4)	2.98	3.01	<0.006	4.91	798	105
R5(S5)	3.19	3.20	<0.006	3.40	546	71.7
R5(S6)	3.54	3.46	<0.006	1.66	651	75.2
R5(S7)	4.88	4.28	<0.006	0.245	284	15.8
R5(S8)	5.19	4.96	<0.006	0.184	451	15.7
R5(S9)	5.61	5.61	<0.006	0.039	207	3.30

Thermal analysis (TG-DSC) results for R1(S1) and R1(S9) are shown in **Figure 3.1**. The sample formed at the highest pH (~5.7) and SO_4:Fe=1, R1(S9), shows three stages of weight loss, with a total weight loss of ~19% at approximately 800 °C. The first stage (T1) shows a gradual weight loss, with a corresponding broad endothermic DSC peak centered at ~105 °C. Weight loss up to this temperature is normally attributed to the evaporation of non- structural water trapped in the interstitial spaces of aggregated particles and associated loosely with particle surfaces. The majority of weight loss associated with the second stage (T2) occurs over a relatively narrow temperature interval, 220-280 °C, with a sharp endothermic DSC peak at ~250 °C, possibly due to the loss of structural water associated with a phase transition. A gradual weight loss (2 - 3 % of the total) from approximately 280 to 600 °C may be associated with continued diffusion-limited release of structural water after the phase transition. Therefore, we define T2 weight losses as occurring between 220 and ~600 °C. The T1 and T2 stages account for ~80% of the total weight loss in R1(S9). The third stage (T3) of weight loss is relatively small and occurs over a broad temperature interval, 610 - 800 °C, and is not accompanied by a strong or clearly delineated DSC peak. This stage of weight loss is likely associated with sulfate decomposition to SO_3 gases.

The sample formed at the lowest pH (~2.5) and SO_4:Fe=1, R1(S1), shows four stages of weight loss, with a total weight loss of ~31% at ~800 °C (**Figure 3.2**). The T1 stage again shows a smooth weight loss, with a broad endothermic DSC peak centered at ~120 °C, slightly higher than observed for R1(S9). R1(S1) shows no sharp endothermic DSC at ~255 °C, as was observed from 220 – 280 °C in stage T2 for R1(S9), but instead shows a broad, asymmetric endothermic DSC peak extending up to ~340 °C, with a corresponding gradual weight loss up to ~600°C. Weight losses over this entire temperature interval account for ~70% of the total weight loss in R1(S1), and are likely attributable to losses of both loosely bound and structural water. Stage T3 in R1(S1) occurs over a relatively narrow temperature interval, 600 - 680 °C, with a strong, sharp endothermic DSC peak at ~670 °C. As in sample R1(S9), this stage of weight loss is likely associated with sulfate decomposition to SO_3 gases. The weight losses associated with T3 are larger in R1(S1) compared with R1(S9), possibly indicated that R1(S1) has a higher amount of sulfate. A relatively minor second endothermic DSC peak is noted at ~630 °C, slightly lower than the temperature associated with sulfate decomposition. This DSC peak corresponds with the

first of two inflection points in the TG curve over this temperature interval, and is likely attributable to weight losses associated with a final stage of sample dehydration. Therefore, we use this feature at ~630 °C as the boundary between T2 and T3. **Table 3.2** includes weight losses for each of the three stages in samples R1(S1-S9).

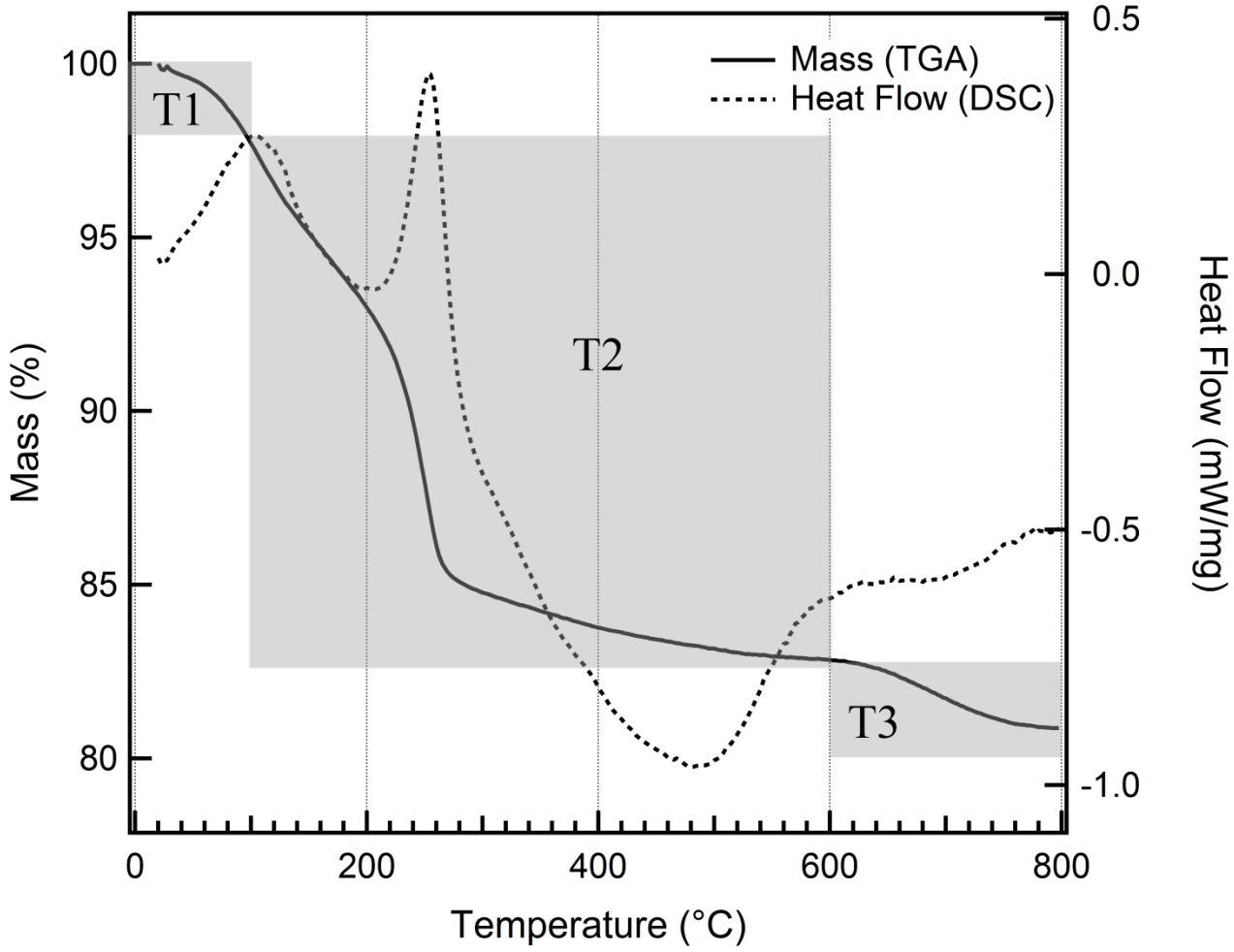

Figure 3.1. TGA-DSC curves for R1(S9).

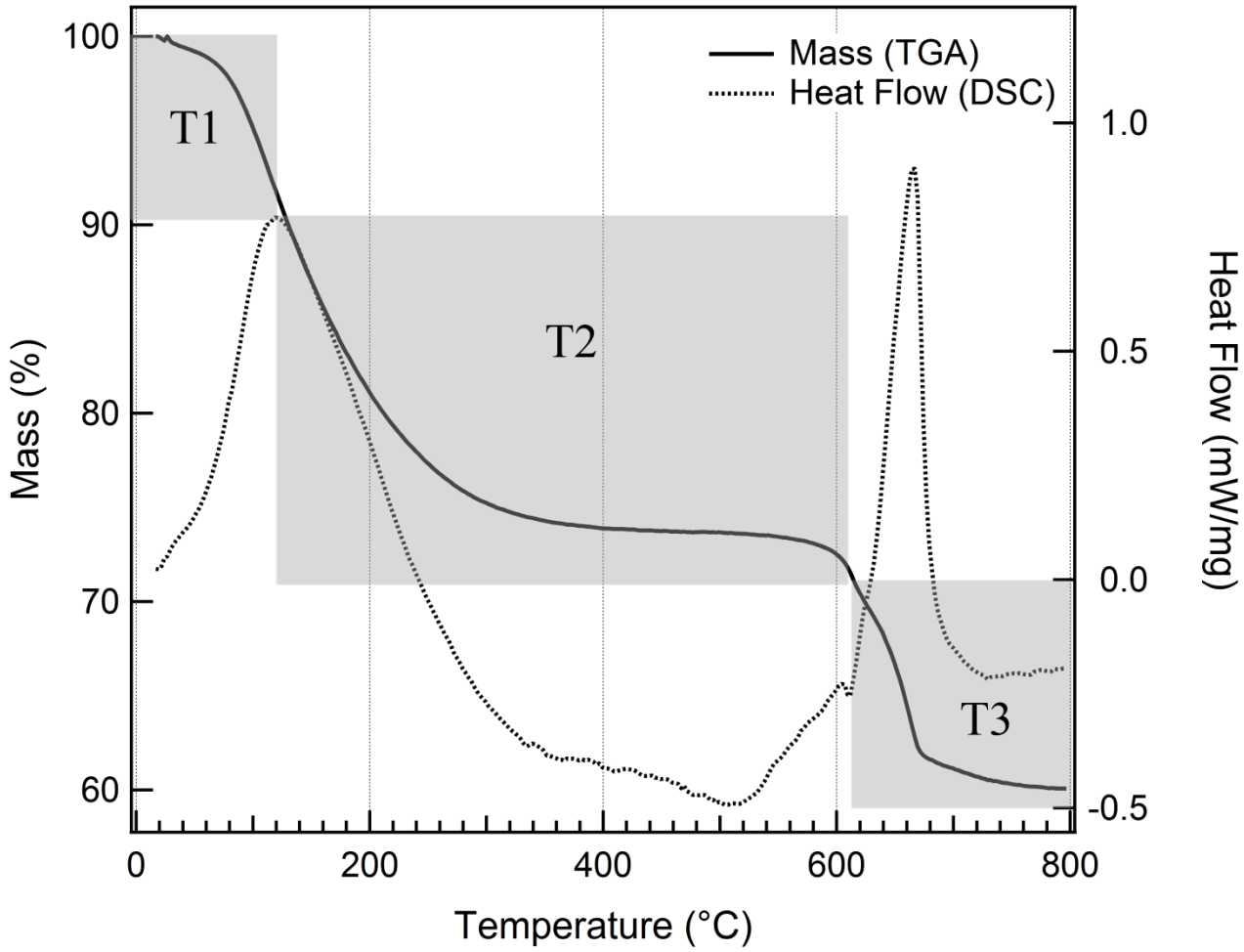

Figure 3.2.TGA-DSC curves for R1(S1).

Table 3.2. Percent weight loss from thermal analysis of samples formed at SO_4:Fe=1.0 and pH ranging from 2.44 – 5.62.

Sample ID	Mineral Phase	T1 %	T2 %	T3 %
R1(S1)	S	7.6	17.9	10.8
R1(S2)	S	6.0	16.9	9.9
R1(S3)	S	6.4	19.0	11.9
R1(S4)	S	6.3	15.2	12.5
R1(S5)	S	5.9	15.7	12.5
R1(S6)	S, L, Gt	5.6	16.2	11.5
R1(S7)	S, L, Gt	3.7	9.2	11.1
R1(S8)	S, L, Gt	2.4	7.7	6.5
R1(S9)	Gt	2.3	7.9	5.9

TG and DSC curves for the entire series formed at SO_4:Fe = 1 are shown in **Figures 3.3 and 3.4**, respectively (individual TG-DSC plots for all samples analyzed are included as **Appendix A**). TG curves for this series show that the total weight loss at ~800 °C for the samples generally decreases with increasing synthesis pH. The DSC curves show several broad endothermic (positive) peaks that change position and intensity with increasing synthesis pH. The DSC curves for the samples formed at pH <2.9 have features that are most similar to R1(S1). DSC curves for the higher synthesis pH (>4.78), intermediate samples have features that are most similar or R1(S9). Intermediate samples R1(S6) and R1(S7) appear to show features that are a combination of the endmembers. The center of the endothermic DSC peak associated with the T1 stage of weight loss shifts to slightly lower temperature for the samples formed at pH ~3.95 and above (R1(S7) through R1(S9)), possibly indicating a change in the strength of the interaction and/or the release rate of the loosely bound water associated with the solid. There is also a decrease in DSC peak intensity for these same samples, suggesting a decrease in the amount of loosely bound water for these samples. The intensity of the endothermic DSC peak centered ~250 °C and corresponding to the T2 stage of weight loss increases from R1(S7) to R1(S8), indicating an increase in the relative proportion of the R1(S9) endmember in these samples. Likewise, the decreasing intensity of the main endothermic DSC peak associated with the T3 stage of weight loss suggests that the relative proportion of the R1(S1) endmember is decreasing in these samples with increasing pH.

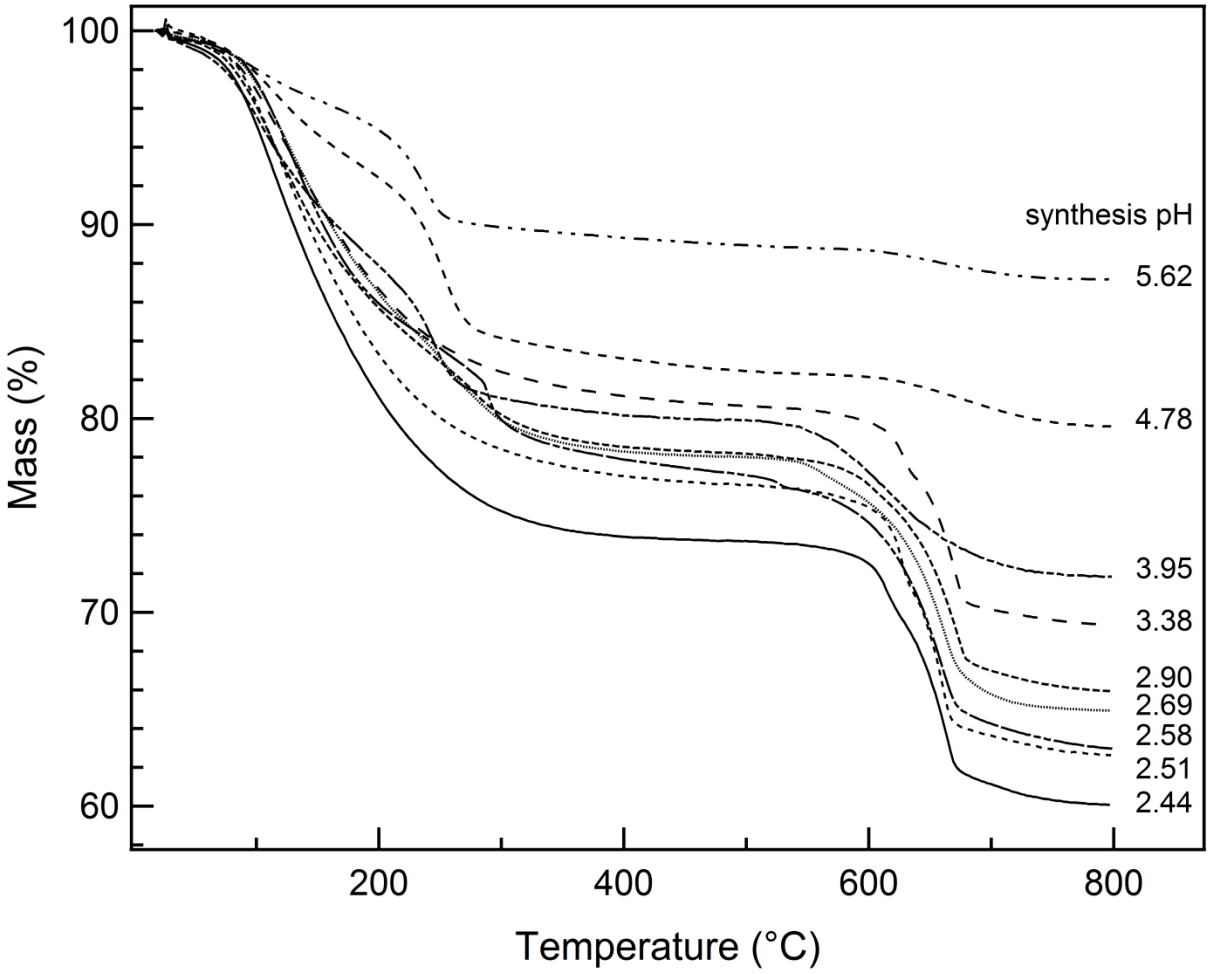

Figure 3.3. TG curves of R1(S1-S9)

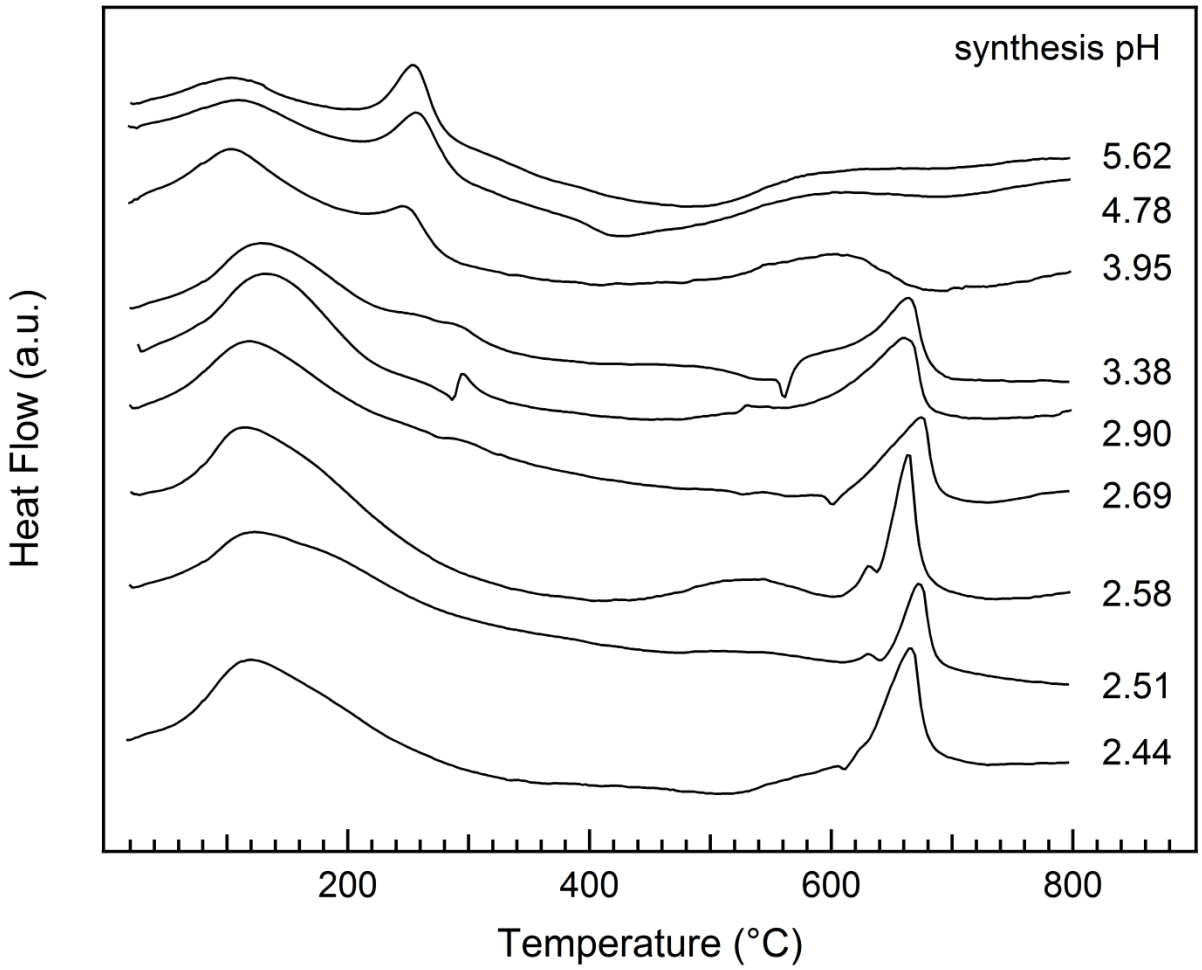

Figure 3.4. DSC curves of R1(S1-S9)

TG and DSC curves for samples R5(S1-S5) formed at pH <3.2 are shown in **Figures 3.5 and 3.6**. TG-DSC plots for all samples analyzed are given as **Appendix A**. DSC curves for these samples appear to show different behavior during heating, most notably the lack of a first strong endothermic DSC peak centered at ~110 °C that would be normally attributed to the loss of loosely bound water. This is because, in contrast to samples formed at SO_4:Fe = 1 and described above, samples R5(S1-S5) were pre-heated in an oven in order to remove loosely bound water prior to thermal analysis (see Methods section and text below for additional details). Despite this difference, R5(S1-S5) show similar overall behavior to the T2 stage of samples R1(S1-S5) in that they undergo a smooth, continuous weight loss up ~600 °C that is likely attributable mainly to loss of structural water. The strong endothermic DSC peak associated with the T3 stage of weight loss is also present in R5(S1-5), and is attributed to sulfate decomposition to SO_3 gases.

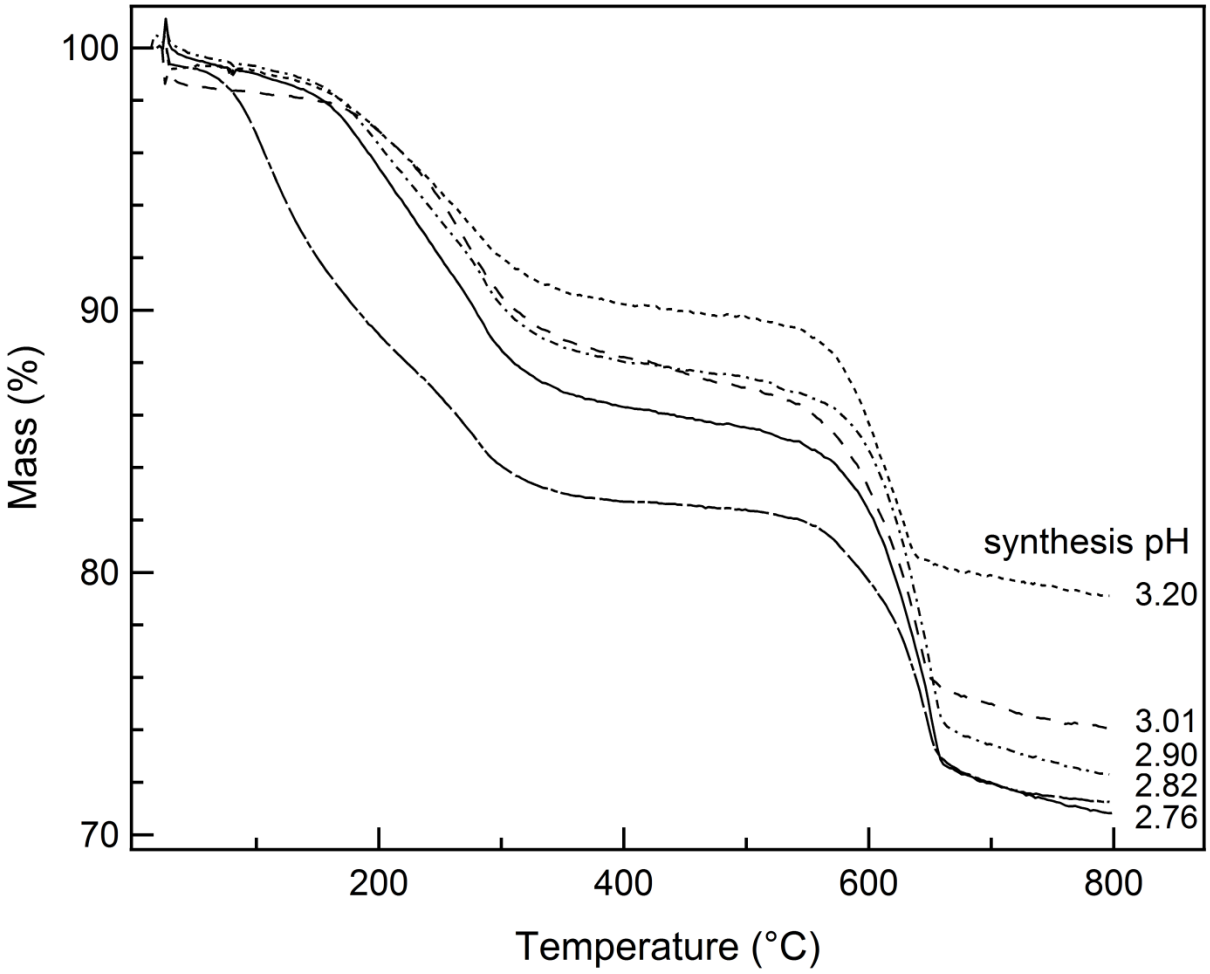

Figure 3.5. TG curves of R5(S1-S5)

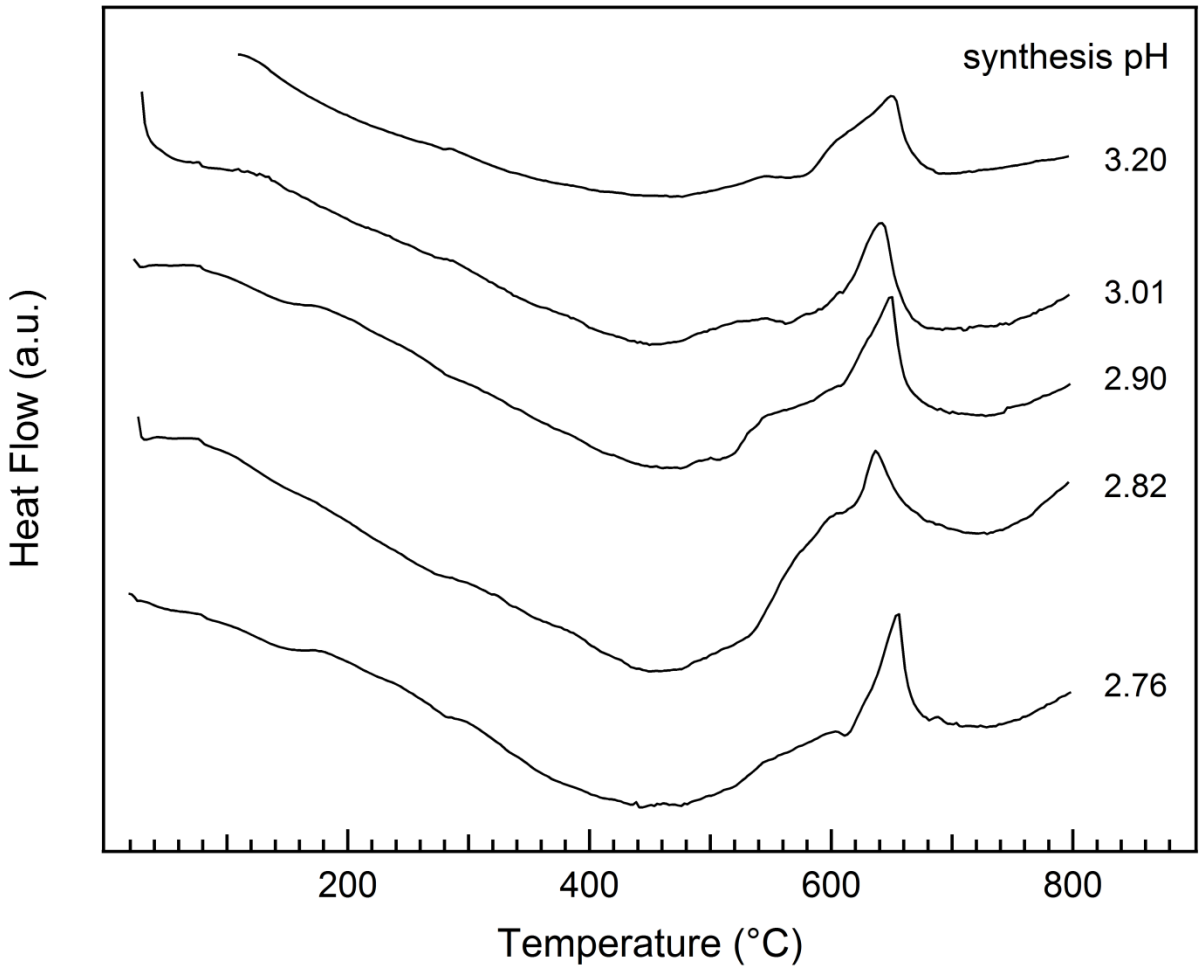

Figure 3.6. DSC curves of R5(S1-S5)

The effects of pre-heating samples to remove loosely bound water prior to thermal analysis are illustrated by TG and DSC curves for R1(S3) in **Figure 3.7**. TG curves for R1(S3) with and without pre-heating have a difference of 1.8% in the total weight loss at ~800 ºC. The changes in the TG curves are similar from ~20-800 ºC, but magnitude of weight loss is not the same with and without pre-heating. The most significant difference is in the T2 stage of weight loss up to ~640 ºC, which is less in the pre-heated samples by 2 – 3%. Duplicate runs of R1(S3) demonstrate the reproducibility of the pre-heating method. Corresponding DSC curves for R1(S3) with and without pre-heating show similar overall behavior in the T2 and T3 stages. However, the two pre-heat R1(S3) samples both show a small endothermic DSC peak centered at ~200 ºC, which possibly is due to residual amounts of loosely bound water that was not removed by pre-heating or was taken up by the samples during cooling in the oven and/or during transfer

from the oven to the TG-DSC. Total mass loss data for pre-heated samples are included in **Table 3.3.**

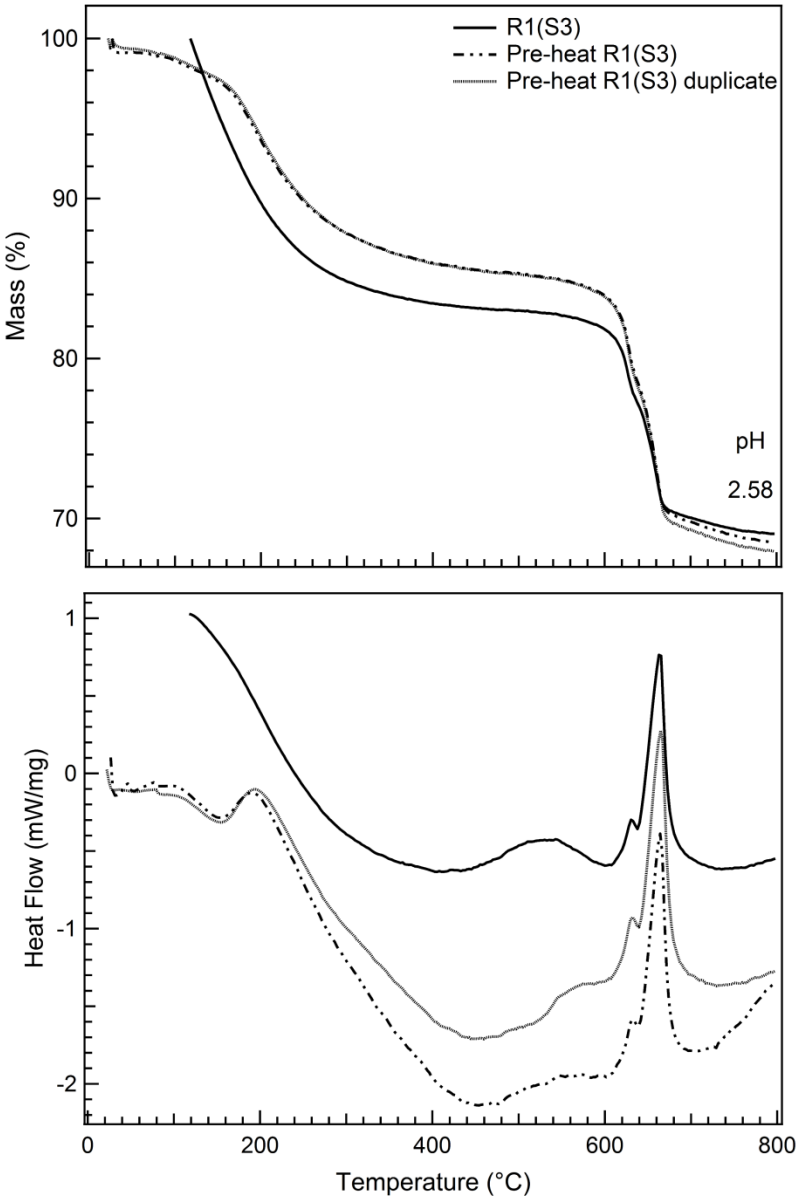

Figure 3.7. TG and DSC curves of R1(S3) with and without pre-heating and a duplicate of R1(S3) with pre-heating.

Table 3.3. Percent weight loss from thermal analysis of samples in the SO_4:Fe=1 and 5 series with pre-heating in an oven. We assumed no T1 weight losses due to pre-heating.

Sample ID	Mineral Phase	T1 %	T2 %	T3%
R1(S1)	S		16.7	12.4
R1(S3)	S		18.5	13.5
R1(S3) duplicate	S		18.9	12.6
R1(S4)	S		14.3	10.0
R1(S4) duplicate	S		14.3	12.5
R5(S1)	S		16.8	8.9
R5(S2)	S		13.9	6.8
R5(S3)	S		20.5	8.0
R5(S4)	S		15.2	7.9
R5(S5)	S		16.1	6.7

3.2 Bulk X-ray Diffraction Characteristics

Synchrotron X-ray diffraction (XRD) data for R1(S1-S9) and R5(S1-S9) are shown in **Figures 3.8 and 3.9**, respectively. The two samples precipitated at the lowest pH in each series, R1(S1) and R5(S1), each show approximately eight broad peaks centered at d-spacings of approximately 1.46, 1.51, 1.68, 1.97, 2.33, 2.56, 3.40 and 4.89 Å. Similar XRD characteristics are observed for samples R1(S2-S5) and R5(S2-S5). Such peak broadening generally results from lack of long-range structural order or small particle size. In contrast, the two samples precipitated at the highest pH in each series, R1(S9) and R5(S9), each show at least 20 relatively narrow, well-defined XRD peaks (**Figures 3.8 and 3.9**). Comparing the XRD profiles for the whole series, we find peaks are more intense, sharper and better resolved with increasing synthesis pH, suggesting that higher pH increases structural order and degree of crystallinity of the products. With the exception of samples R1(S8) and R5(S8), the XRD peaks in the intermediate samples in both series are generally consistent with the low- and high-pH endmembers, S(1) and S(9), respectively. We observe in XRD data for R1(S8) and R5(S8) additional peaks at 1.90, 3.28 and 6.20 Å that are not present in either endmembers. The large peak width of d=6.20 Å peak suggests that this phase lacks long-range order or has small particle size.

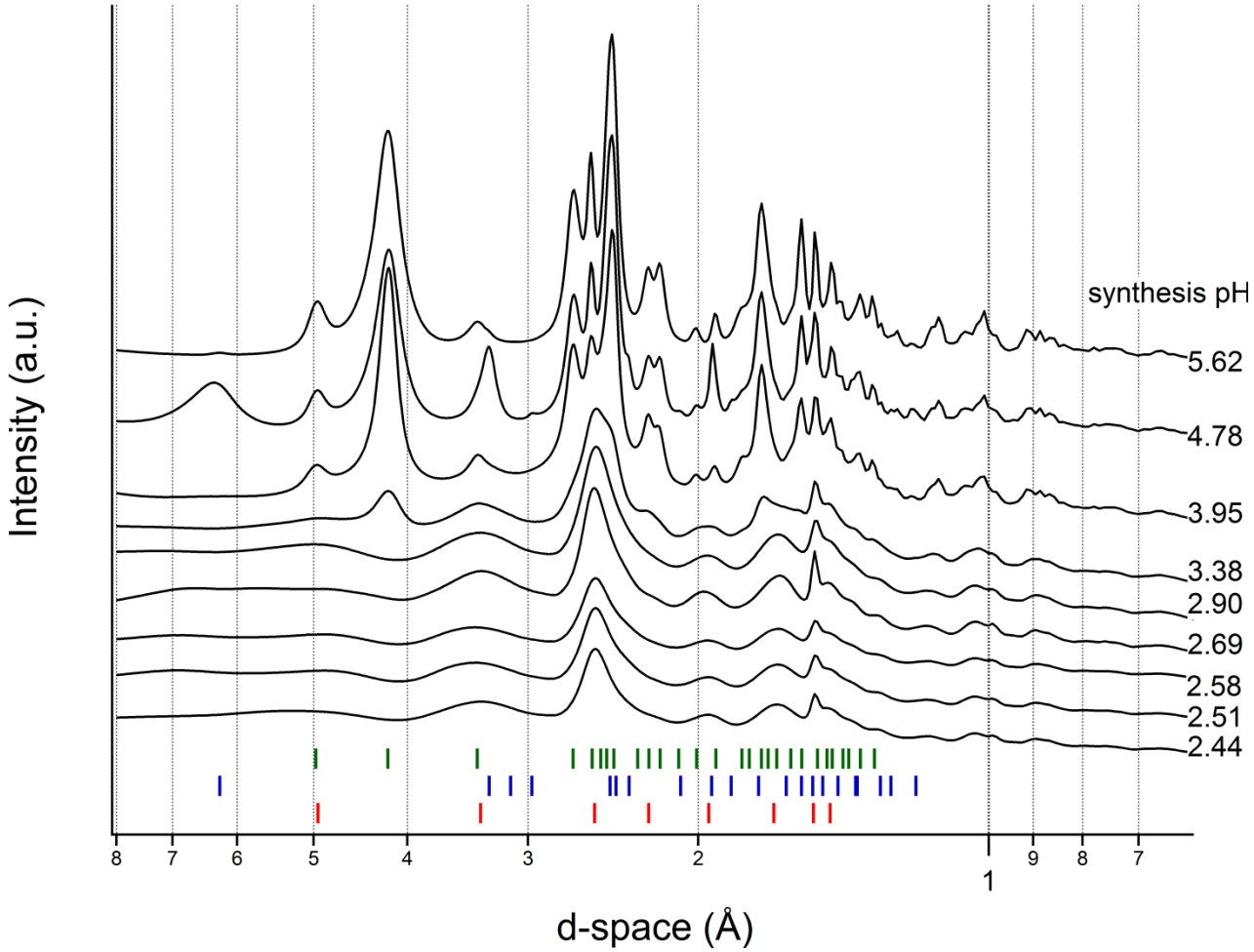

Figure 3.8. Background-subtracted synchrotron powder XRD data with intensity plotted in arbitrary units on the ordinate versus d-space in Å on the abscissa. The samples were synthesized at $[SO_4]/[Fe]=1.0$. pH increases from the bottom to the top. Lower tick marks show the calculated positions of reflections for schwertmannite (bottom, red), lepidocrocite (middle, blue) and goethite (top, green).

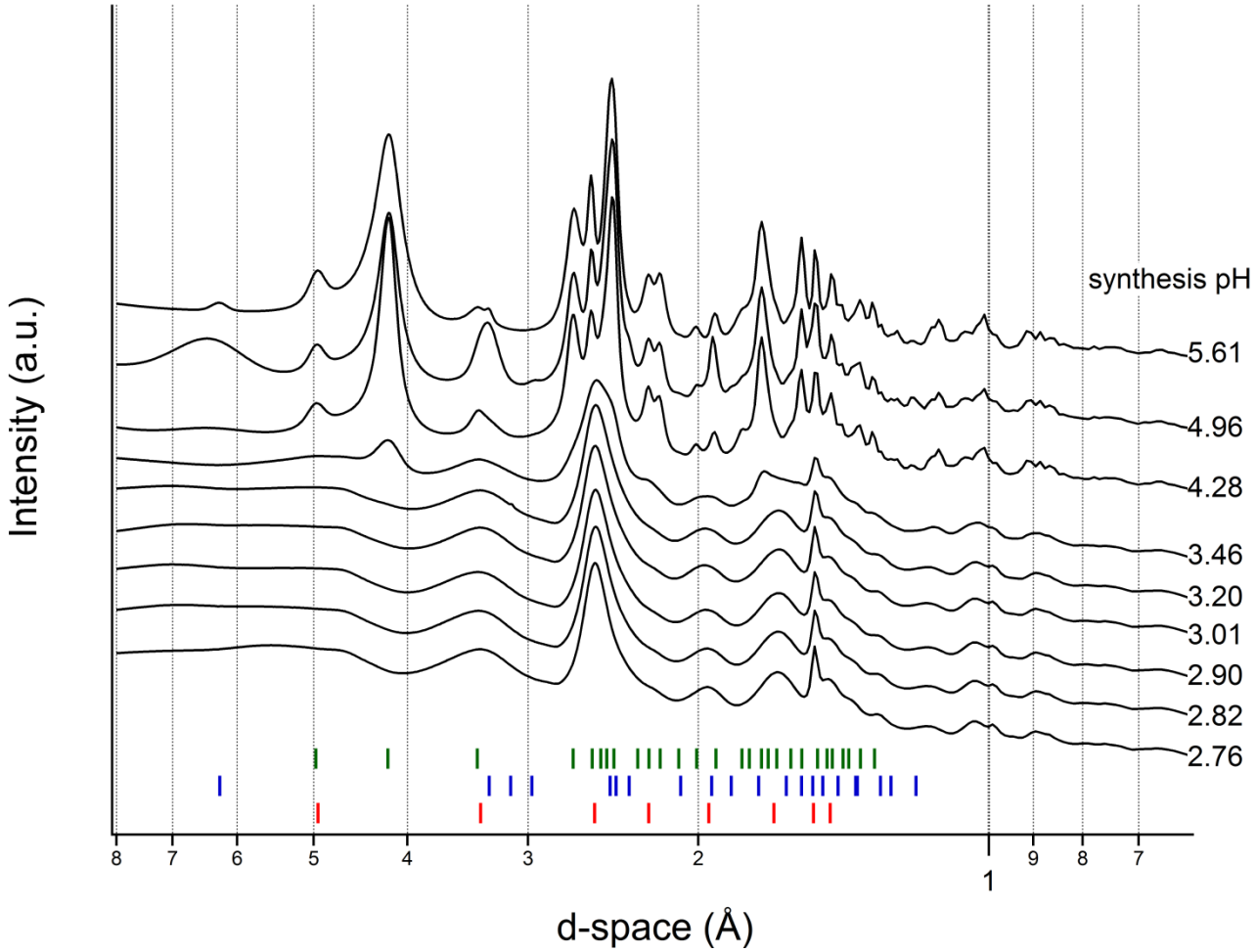

Figure 3.9. Background-subtracted synchrotron powder XRD data with intensity plotted in arbitrary units on the ordinate versus d-space in Å on the abscissa. The samples were synthesized at $[SO_4]/[Fe]=5.0$. pH increases from the bottom to the top. Lower tick marks show the calculated positions of reflections for schwertmannite (bottom, red), lepidocrocite (middle, blue) and goethite (top, green).

We used calculated d-spacings from the XRD peak positions to confirm the different structural phases in each sample of each series. Initially, d-spacings from R1(S1) and R1(S9) were included in the analysis to confirm the identities of the endmembers. For the high synthesis pH sample, R1(S9), the observed peak positions and relative intensities are consistent with those of goethite (α-FeO(OH)). For the low synthesis pH sample, R1(S1), the positions of the 6-8 broad features in the XRD profile are consistent with those reported for schwertmannite. The additional peaks in R1(S8) at d-spacings of approximately 1.90, 3.28 and 6.20 Å suggest a third

distinct phase, which we identify as lepidocrocite (γ-FeO(OH)) based mainly on the first two most prominent XRD peaks at 3.28 and 6.20 Å.

Essentially all of the XRD peak positions in the profiles for R1(S1-S9) are explained by schwertmannite, goethite or lepidocrocite, indicating that each sample is made up of one or more of these phases. Comparison of R1(S1-S9) to R5(S1-S9) shows that similar mineralogical trends are maintained at up to 5 times higher initial solution sulfate concentration for samples formed at similar pH. XRD profiles for R2(S1-S9) and R3(S1-S9), which are included as **Appendix B**, are also virtually identical to the R1 and R5 series.

3.3 XRD Characteristics of Quenched Thermal Analysis Experiments

XRD profiles for portions of sample R1(S2) that were quenched at 400, 500, 600 and 800 °C in four separate TG-DSC runs are shown in **Figure 3.10**. The samples collected at 400 and 500 °C are during the T2 stage of weight loss, the sample at 800 °C is at the end of the T3 stage, and the sample at 600 °C is at the boundary between the two stages (cf. **Figure 3.1 and 3.2**). The sample quenched at the lowest temperature, R1(S2)-400 °C, shows at least three broad peaks centered at d-spacings of ~2.75, ~1.52 and 1.0 Å. R1(S2)-500 °C shows similar features, but also has a series of small, relatively narrow peaks at d-spacings of, for example, ~2.69, ~2.51, ~2.2, ~1.83, ~1.69 and ~1.45 Å. These features become increasingly pronounced in R1(S2)-600 °C and R1(S2)-800 °C, while the intensities of three broad peaks progressively diminish. The observed peak positions and relative intensities for the sample quenched at the highest temperature, R1(S2)-800 °C, are consistent with the hematite (α-Fe_2O_3)pattern.

The XRD patterns for the original R1(S2) (no heating) and the heated and quenched R1(S2) samples show the changes in mineralogy that occur during different stages in the thermal transformation of schwertmannite (**Figure 3.10**). Heating schwertmannite to 400 °C causes an initial decrease in crystallinity, as evidenced by both the decrease in the number of identifiable diffraction peaks and increase in the peak widths. The crystallinity of the sample increases above ~500 °C due to transformation to hematite. Hematite peaks are first observed at 500 °C, and increase in intensity with heating to 600 and 800 °C. The broad features associated with the poorly crystalline intermediate phase steadily diminish and eventually disappear for these same

temperatures. Narrowing of the hematite peaks from 600 and 800 °C indicates an increase in hematite crystallinity.

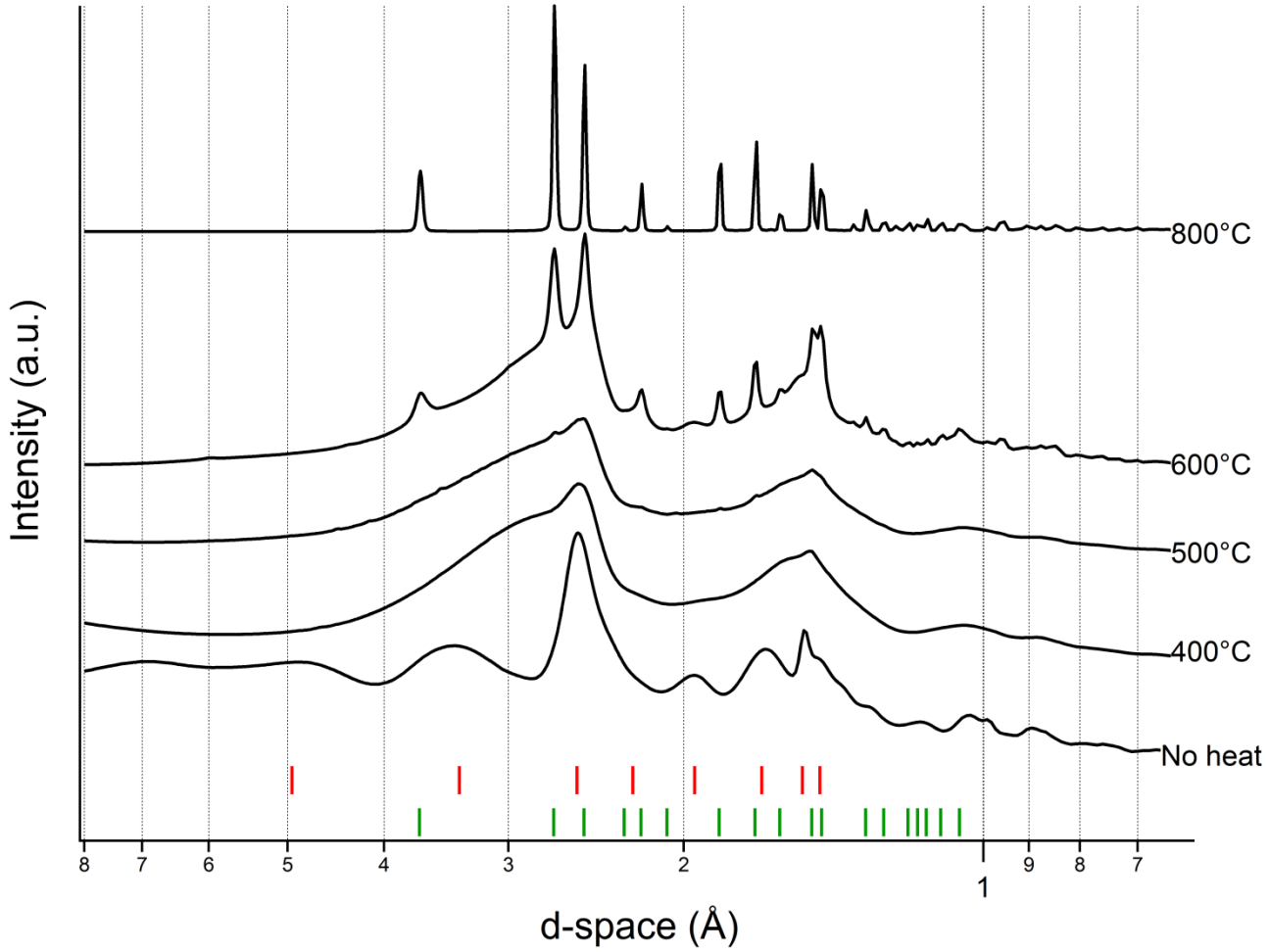

Figure 3.10. Background-subtracted synchrotron powder XRD data for sample R1(S2) prior to ("No heat") and after heating to and quenching at different temperatures of 400, 500, 600 and 800°C during thermal analysis. Lower tick marks show the calculated positions of reflections for hematite (bottom, green) and schwertmannite (top, red).

3.4 SEM and HR-TEM Characteristics

Scanning electron microscopy (SEM) images for selected samples R1(S1, S3, S7 and S9) are shown in **Figure 3.11**. Samples R1(S1) and R1(S3), identified as pure schwertmannite by XRD, consist of rounded particles with average diameters in the range of 250-400 nm (**Figures 3.11A and 3.11B**). Sample R1(S7) consists of similarly sized rounded particles, although these appear to have coalesced into larger aggregates (**Figure 3.11C**), possibly due to artifacts associated with

drying and/or because XRD results indicate that it is a mixture of poorly crystalline goethite and residual schwertmannite. In contrast, the sample precipitated at the highest pH, R1(S9), shows elongated, needle-like particles that are ~20-60 nm in length and ~5 nm in width (**Figure 3.11D**). The shape and size of the observed particles are typical of what is normally reported for laboratory-synthesized goethite, which was confirmed by XRD to be the dominant phase in R1(S9).

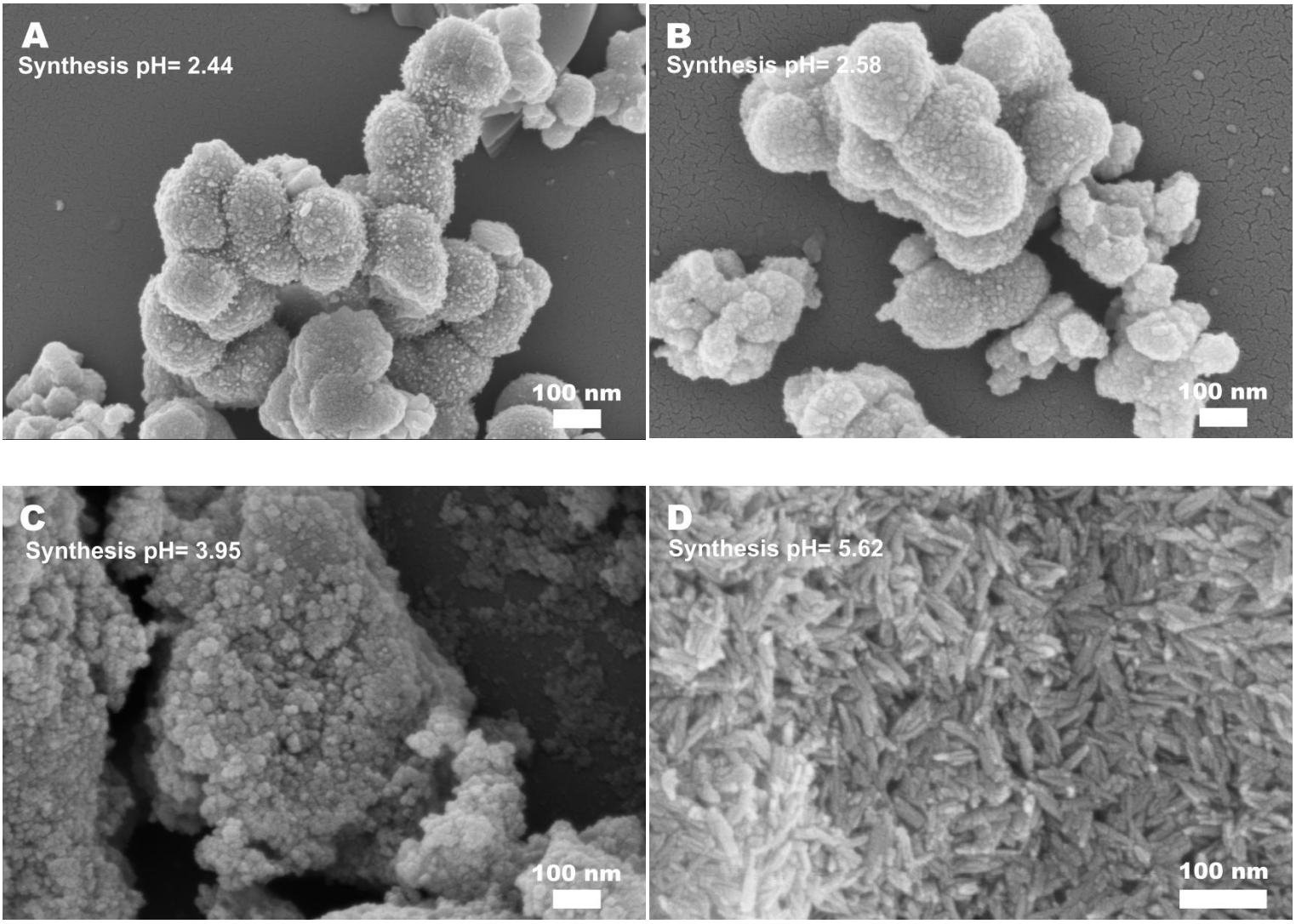

Figure 3.11. SEM images of S1-1(A), S1-3 (B), S1-7 (C) and S1-9 (D).

Figures 3.12-3.14 show high-resolution transmission electron microscopy (HR-TEM) images and fast Fourier transform (FFT) patterns for R1(S1, S3, S7 and S9). Sample R1(S9) was

also analyzed by selected area electron diffraction (SAED). Consistent with SEM results, a low-resolution survey image of R1(S1) shows round shaped schwertmannite particles of ~300 nm in diameter (**Figure 3.12A**). Higher resolution images (**Figure 3.12B**) reveal that the schwertmannite particles are aggregates of smaller partially crystalline nanodomains that appear embedded in an amorphous matrix. These nanocrystalline domains are approximately 3-5 nm in diameter, are round to slightly elongated in shape, and have visible lattice fringes. The surrounding material is considered amorphous due to the apparent lack of lattice fringes or evidence of crystal facets. FFT patterns of selected areas containing the nanocrystalline domains (**Figure 3.12C and D**) indicate d-spacings of 2.25, 2.56 and 2.69 Å. These values are compared in **Table 3.4** to d-spacings reported previously for schwertmannite and to those calculated for goethite and lepidocrocite.

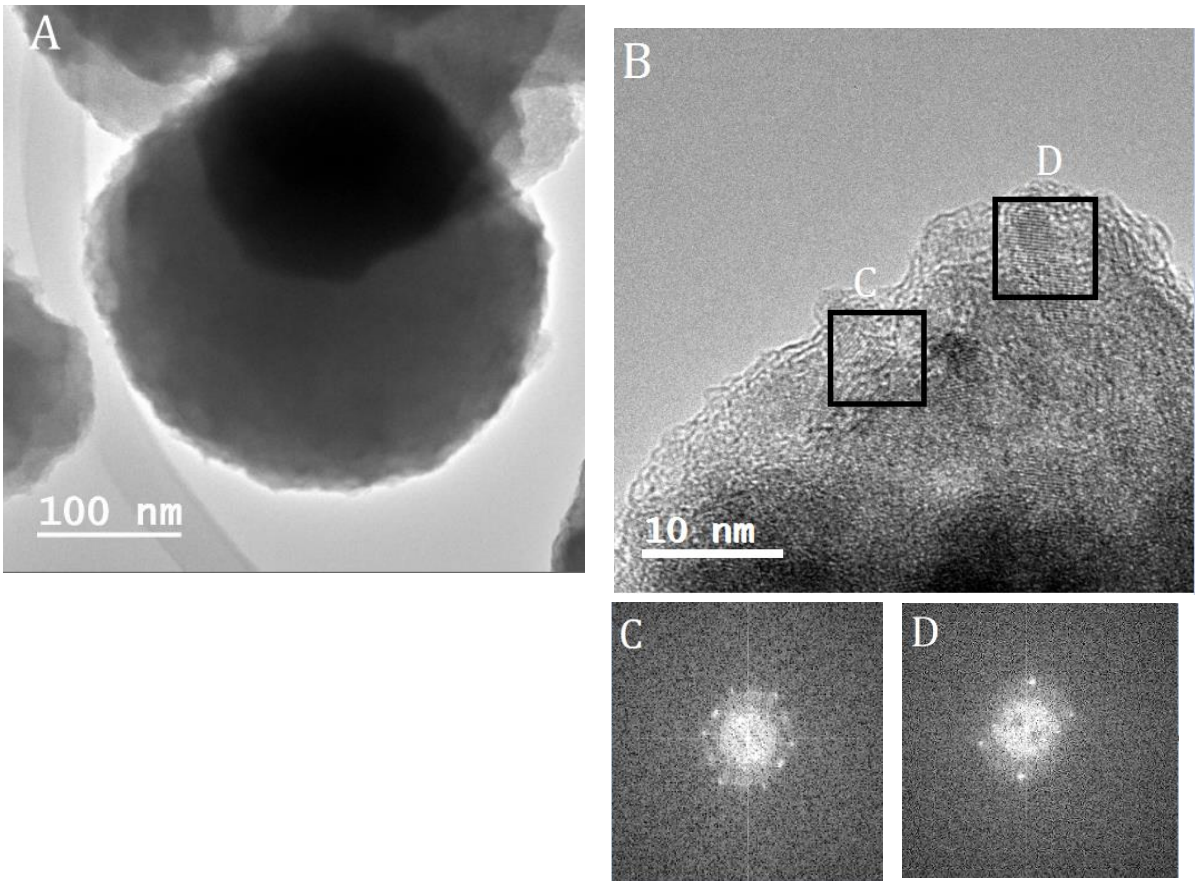

Figure 3.12. TEM images of R1(S1) showing (A) rounded aggregates at low-resolution and (B) partially crystalline nanodomains. FFT patterns (C and D) calculated from boxed areas shown in image B.

TEM images of R1(S3) indicate that the schwertmannite in this sample also consists of rounded aggregates that, at high resolution, are mixtures of partially crystalline nanodomains embedded in an amorphous matrix (**Figure 3.13**). Interestingly, R1(S3) also has needle-like protrusions that extend ~20-25 nm from the particle surfaces (**Figure 3.13A**). This so-called "pin-cushion" morphology for schwertmannite has been reported previously in studies of natural and synthetic samples using HR-TEM and SEM analyses (Bigham and Nordstrom 2000; Bigham et al. 1994; French et al 2012,2013). Measured d-spacing from FFT patterns (**Figure 3.13C and D**) of nanocrystalline domains located in the needle-like protrusion in sample R1(S3) are included in **Table 3.4**. Overall the calculated d-spacings are similar to what we find for R1(S1) suggesting that the observed nanodomains have structural characteristics most similar to goethite.

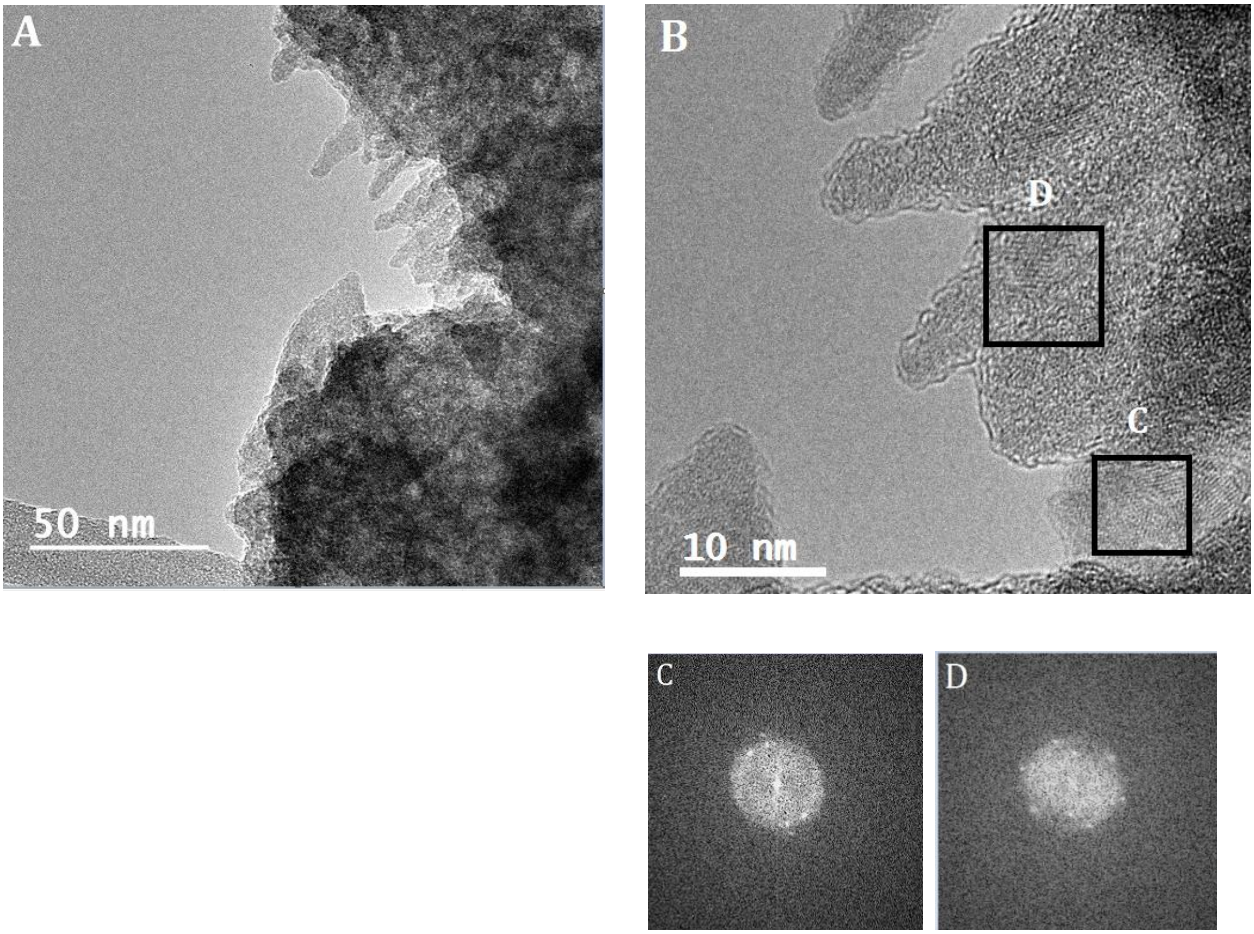

Figure 3.13. TEM images of R1(S3) showing schwertmannite's needles growing off the surface of the particle (A) and nanocrystalline domains (B). FFT patterns (C and D) show measured d-spacings from the areas in squares (B).

The HR-TEM results for R1(S9) are shown in **Figure 3.14**. Consistent with SEM results, the sample consists of densely packed needles of ~30-60 nm in length are shown in **Figure 3.14A**. Imaging at high-resolution (**Figure 3.14B**) shows that the individual needles have visible lattice fringes indicating that they are nanocrystalline. Some needles appear to be made of aggregates of nanocrystals. Measured d-spacing from FFT patterns (**Figure 3.14C and D**) of nanocrystalline domains located in the needle-like protrusion in sample R1(S9) are consistent with goethite (**Table 3.4**). This finding was confirmed by d-spacings measured from visible diffraction rings in the SAED pattern (**Figure 3.14F**). These values are also included in **Table 3.4**.

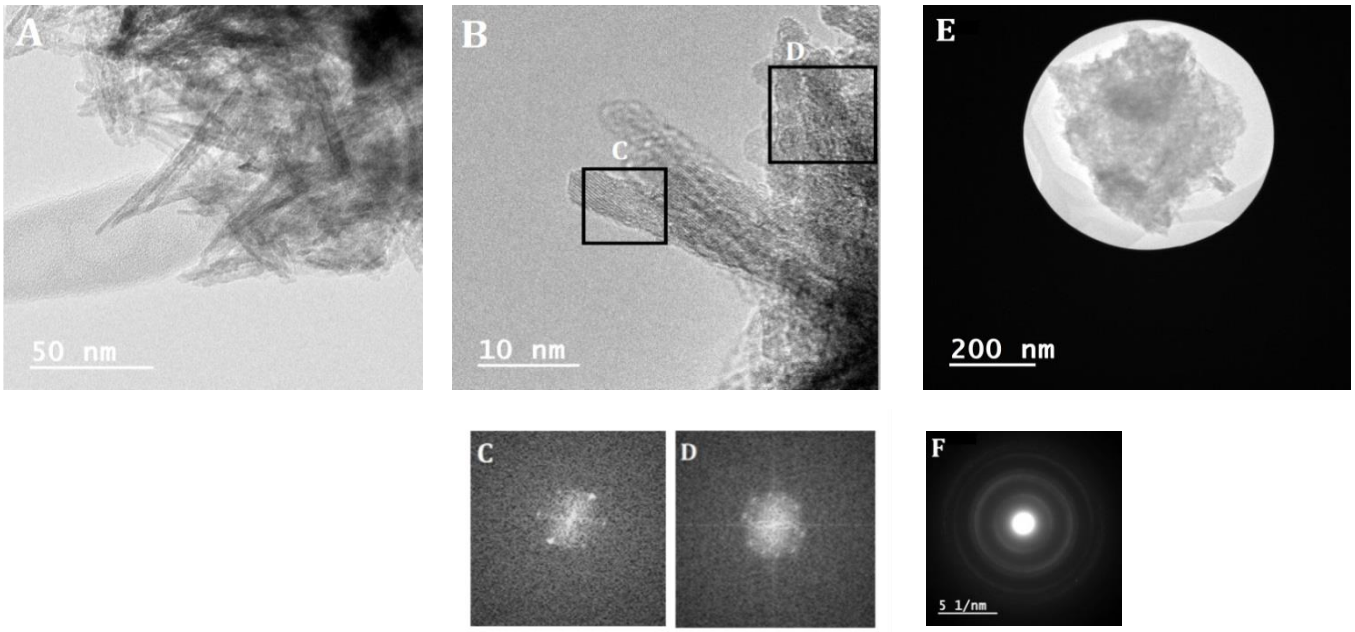

Figure 3.14. TEM images of R1(S9) showing goethite needles (A) and nanocrystalline areas on densely packed goethite needles (B). FFT patterns (C and D) show measured d-spacings from the squares in (B). Image (F) shows a SAED pattern of image (E).

Table 3.4. Measured d-spacings from FFT and SAED analysis on R1(S1, S3 and S9).

Sample ID	pH	Box	Mineral Phase	Analysis	Observed d-spacing (Å)	*Reference S d-spacing (Å)	*Reference Gt d-spacing (Å)	hkl	2-θ
R1(S1)	2.44	C	Gt	FFT	2.245	-	2.253	(121)	40.0
		C	S	FFT	2.561	2.56	-	(212)	35.2
		C	Gt	FFT	2.699	-	2.693	(130)	33.4
		D	S	FFT	2.561	2.56	-	(212)	35.2
R1(S3)	2.58	C	Gt	FFT	2.220	-	2.190	(140)	41.2
		C	Gt	FFT	2.699	-	2.693	(130)	33.4
		D	Gt	FFT	2.220	-	2.190	(140)	41.2
		D	Gt	FFT	2.436	-	2.450	(111)	36.3
		D	S	FFT	2.561	2.56	-	(121)	35.2
R1(S9)	5.62	C	Gt	FFT	2.594	-	2.583	(021)	34.8
		C	Gt	FFT	2.699	-	2.693	(130)	33.4
		D	Gt	FFT	2.594	-	2.583	(021)	34.8
		D	Gt	FFT	2.699	-	2.693	(130)	33.4
		F	Gt	SAED	2.245	-	2.253	(121)	40.0
		F	Gt	SAED	2.466	-	2.450	(111)	36.8
		F	Gt	SAED	2.699	-	2.693	(130)	33.4
		F	Gt	SAED	4.158	-	4.183	(110)	21.2

*Reference schwertmannite (S) and goethite (Gt) d-spacings from Bigham et al. (1996)

4. DISCUSSION

4.1 Schwertmannite synthesis

The results of laboratory-based studies of schwertmannite are difficult to interpret partly because different synthesis conditions (e.g., temperature, concentration, oxidizing agent, etc.) seem to produce differences in the crystallinity and composition of the solid. Various schwertmannite synthesis methods have been used in past studies, which are summarized here and in **Table 4.1**. A number of studies (e.g., Brady et al., 1986; Bigham et al., 1990; Yu et al., 2002, Fernandez-Martinez et al., 2010) used a protocol involving synthesis at elevated temperature of 60 to 85°C with pH ranging from ~2.1 to 6.0. Those authors along with Loan et al (2002), Yu et al (2002) and Reinsch et al (2010) started the experiment with a ferric sulfate solution. Regenspurg et al. (2004) and French et al. (2012, 2014) oxidized ferrous sulfate to ferric sulfate at room temperature using hydrogen peroxide. Synthesis times varied from hours to weeks. Drying procedures ranged from room temperature in air to 40 to 60°C in an oven to freeze-drying. Schwertmannite was identified as the final precipitate based on its characteristic laboratory XRD pattern. However, the patterns have low signal-to-noise ratio that is due partly to the poor crystallinity of the schwertmannite, as well as to the relatively low intensity of the conventional

laboratory X-ray source (for example, see Regenspurg et al., 2004). The degraded quality of the laboratory XRD patterns precludes detailed comparison of the effects of synthesis conditions on schwertmannite crystallinity. Thus, although it appears that schwertmannite can be formed in a variety of ways, this does not guarantee that these synthetic materials have identical crystallinity and composition, or that they are similar to schwertmannite formed in nature.

Table 4.1. Summary of various schwertmannite synthesis methods from reported literature.

Ref	Fe reagent	Oxidizing agent	pH adjustment reagent	Synthesis temperature and time	Sample drying procedure
1	$Fe_2(SO_4)_3 \cdot xH_2O$			85 °C for 1 h	Oven dried at 60 °C for 24 h
2	$(NH_4)_2Fe(SO_4)_2 \cdot 6H_2O$	H_2O_2	NaOH		Oven dried at 40 °C
3	$FeSO_4 \cdot 7H_2O$	H_2O_2			Air
4	$FeSO_4 \cdot 7H_2O$	H_2O_2	Na_2SO_4	75 °C for 24 h	Air
5	$Fe(NO_3)_3 + Na_2SO_4$		H_2SO_4	60 °C for 12 min	Freeze
6	$FeSO_4 \cdot 7H_2O$	Bacteria			Freeze
7	$Fe(NO_3)_3 \cdot 9H_2O + K_2SO_4$			60 °C for 12 min	Air
8	$Fe_2(SO_4)_3 \cdot xH_2O$			85 °C for 1 h	Freeze
9	$Fe^{3+} + Na_2SO_4$			60 °C for 12 min	Freeze and air
10	$Fe(NO_3)_3 + Na_2SO_4$		Na_2SO_4	60 °C for 12 min	Freeze
11	$Fe(NO_3)_3 \cdot 9H_2O + Na_2SO_4$			60 °C for 12 min	Oven dried at 50 °C
12	$FeCl_3 + Na_2SO_4$			75 °C	Anaerobic glovebox
13	$FeSO_4 \cdot 7H_2O$	H_2O_2			Freeze

1) Loan et al. (2004)
2) Davidson et al. (2008)
3) French et al. (2014) (1st synthesis)
4) French et al. (2014) (2nd synthesis)
5) Bigham et al (1990)
6) Bigham et al (1996a)
7) Bigham et al (1996b)
8) Hockridge et al (2009)
9) Fernandez-Martinez (2010)
10) Brady et al. (1986)
11) Yu et al (2002)
12) Reinsch et al. (2010)
13) Regenspurg et al (2004)

Our approach was to synthesize Fe-(oxy)hydroxides and hydroxysulfates at initial solution conditions that are more nearly representative of natural environments. In our experiments, the initial ferrous iron concentration, 72 mM, and sulfate concentrations, 72 – 360 mM, are within the ranges commonly reported for acid mine drainages. Ferrous sulfate was completely oxidized to ferric sulfate by the addition of a dilute oxidizing agent (H_2O_2, 0.15% wt/wt). The pH range studied (approximately 2.4 to 5.6) overlaps with the pH range of 2 to 4 that is typically associated with schwertmannite formation (Bigham et al., 1992). Synthesis time was fixed at approximately 24 hours, and sample synthesis, aging, washing and drying were all done at room temperature. In addition to systematically varied synthesis conditions, we used the systematic application of complementary analytical characterization methods to examine to what extent varying initial solution chemistry affected the composition and crystallinity of the products. Synchrotron radiation was used to overcome signal-to-noise issues that are related to low intensity of the X-ray source in laboratory XRD data. Standard spectrochemical analysis (ICP-MS) was used to obtain Fe and S content of the solids. In addition, thermal analysis (TG-DSC) was used to obtain independent estimates of sulfate and water contents in schwertmannite based on mass losses during heating. Electron microscopy complemented bulk measurements by providing direct information on nanoscale crystallinity and morphological characteristics of the solids. By using systematic studies of mineral growth at environmentally relevant conditions, we can more accurately extrapolate the results of laboratory studies to natural conditions.

4.2 Effects of initial solution sulfate [SO_4] and pH on the bulk mineralogy of the entire sample series.

XRD analysis (**Figure 3.8**) showed an abrupt increase in crystallinity at pH ~4 and higher as formation of poorly crystalline schwertmannite is replaced by goethite and minor lepidocrocite. Comparison of the samples formed at different SO_4:Fe ratios ranging from 1 to 5 indicates that initial solution sulfate concentration ([SO_4], 72 – 360 mM) does not significantly impact the overall mineralogy of the solids as a function of pH. Although the pH effect on mineralogy is expected based on previous studies of natural and synthetic Fe-(oxy)hydroxide and hydroxysulfate formation, our analysis of these synthetic samples reveal several interesting results including: 1) the effect of pH on the amount of sulfur incorporation in the solids, 2) the minimal effect initial sulfate concentration has on overall mineralogy, and 3) the occurrence of lepidocrocite in certain samples.

ICP-MS analysis of the solids shows a systematic variation in sulfur content across the entire series of samples formed at SO_4:Fe = 1, 2, 3 and 5 (**Figure 4.1**). The samples can be grouped in two different ways based on bulk composition data: S-enriched samples with high total sulfur, low Fe/S ratio (Group 1) and S-depleted samples with low total sulfur, high Fe/S ratio (Group 2). As shown in Figure 4.1, Group 1 samples have high total sulfur ranging from approximately 1.4 – 2.7 mmol/g and average Fe/S molar ratios ranging from approximately 4.3 to 4.8. Group 2 samples have a relatively narrow range of sulfur contents, 0.1 – 0.5 mmol/g, and large range of Fe/S molar ratios from ~8 – 36 (Table C1 in Appendix).

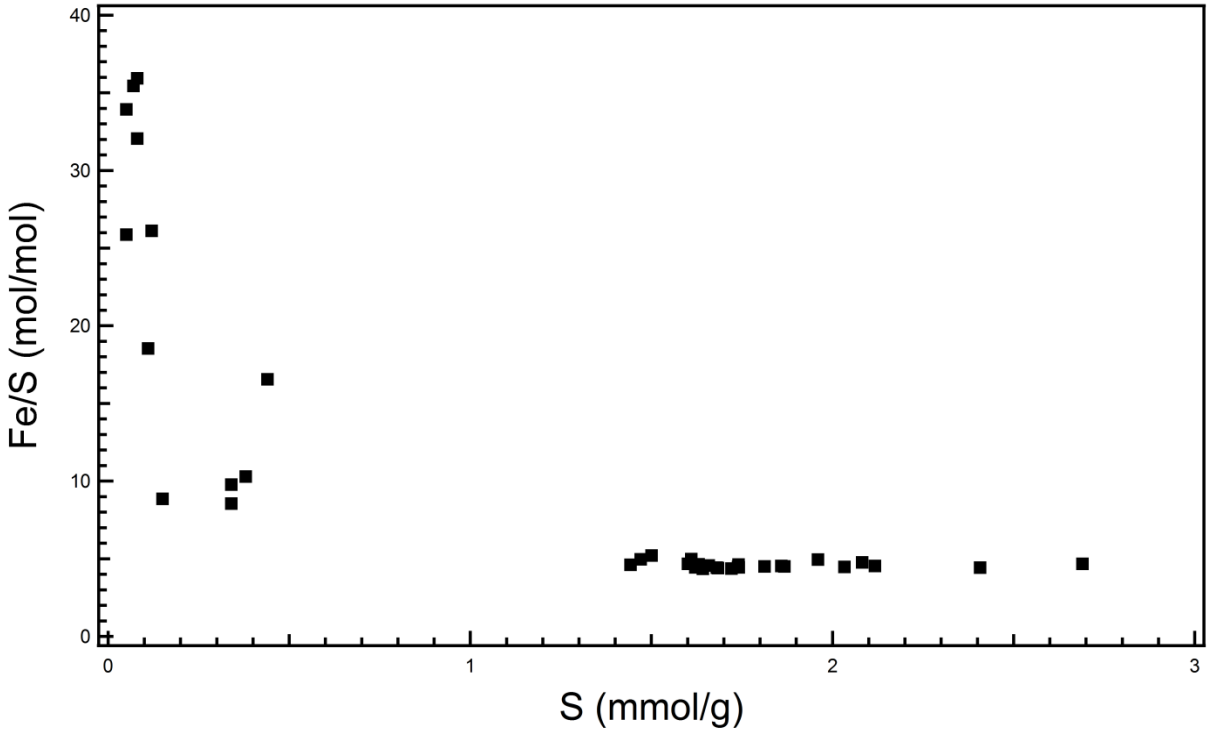

Figure 4.1. ICP-MS data for samples R1, R2, R3 and R5 (S1-S9) plotted as total sulfur (S, mmol/g) versus Fe/S molar ratio. These data are given in Appendix C.

Combined XRD and ICP-MS analyses (**Figure 4.2**) reveal that the two types of behavior are strongly influenced by differences in sample mineralogy. Group 1 samples consist mostly or entirely of schwertmannite and were formed at lower pH in each series (i.e., S1 - S6). Group 2 samples consist mainly of Fe-hydroxides goethite and (minor) lepidocrocite and were formed at higher pH (Table C1 in Appendix). As shown, the Fe/S molar ratio increases with decreasing total sulfur content of the solids. This trend is consistent with the abrupt increases in the total amount of Fe-hydroxide (goethite and lepidocrocite) and sample crystallinity that occurs at pH ~4 and higher. We attribute the apparent gap in samples with bulk sulfur contents from approximately 0.5 – 1.4 mmol g^{-}

[1] to the abrupt change mineralogy, which resulted in relatively few intermediate samples consisting of schwertmannite and goethite in varying proportions. Furthermore, the gap corresponds with the pH regime where the same incremental increase in the amount of sodium bicarbonate added to each synthesis resulted in relatively large increases in pH (**Table 2.1**).

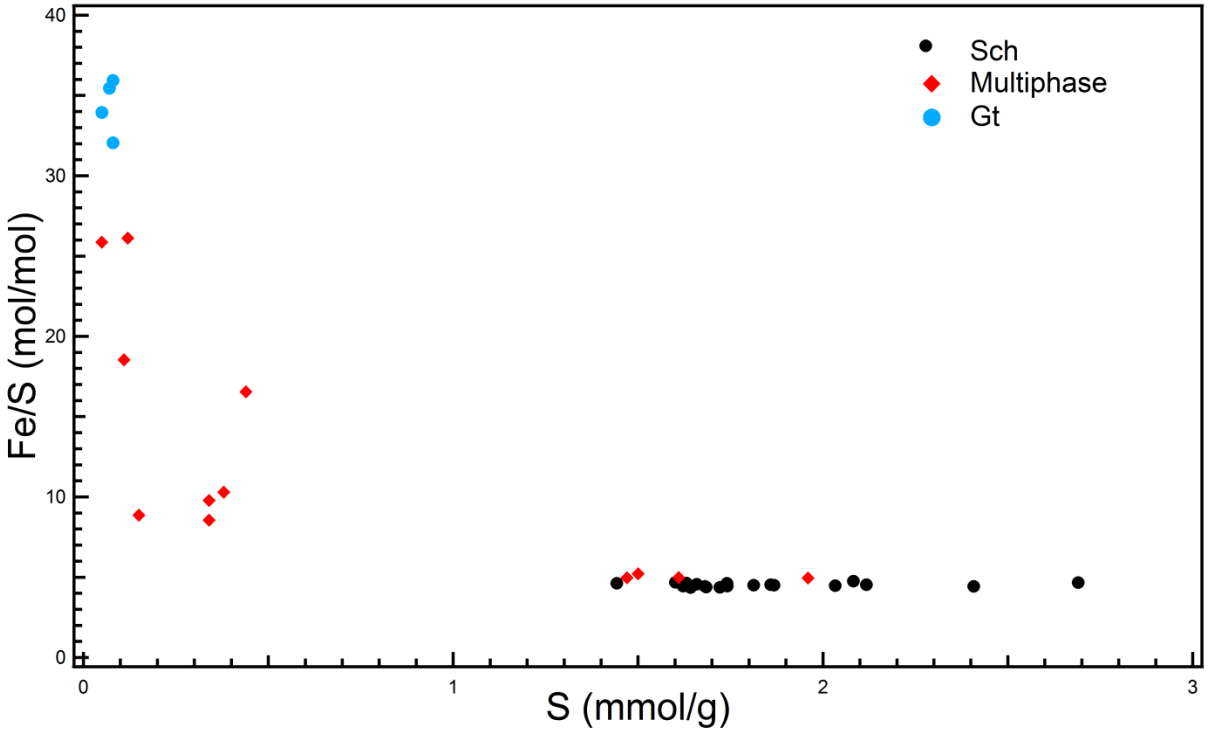

Figure 4.2. Combined ICP-MS and XRD results for samples R1, R2, R3 and R5 (S1-S9). Group 1 consists mostly or entirely of schwertmannite (black squares). Group 2 consists mainly of multiphases (red diamonds) and goethite (blue circles). These data are given in Appendix C.

We predicted that increasing initial solution [SO_4] would suppress goethite and favor schwertmannite formation at increasingly higher pH. However, the results of our synthesis and characterization show that increasing initial [SO_4] by up to 5 times has minimal effect on the overall mineralogy in each sample series. Conversely, increasing pH from ~2.4 to 5.6, which corresponds with an increase hydroxide concentration [OH] by a factor of more than 1,000, has a dramatic effect on mineralogy. Therefore, we attribute the apparent ineffectiveness of sulfate in terms of suppressing goethite formation as being due to the large difference in the magnitude of change of [OH] relative to [SO_4].

XRD analysis showed poorly-crystalline/nanosized lepidocrocite occurring with goethite in S(8) samples formed at pH ~4.8 and at SO_4:Fe ratios ranging from 1 to 5. While goethite is present in samples S(6) through S(9), lepidocrocite is not observed (or is below detection) in flanking samples

S(7) or S(9) formed at lower and higher pH, respectively. This suggests that, relative to goethite, the formation of lepidocrocite is only favorable within a narrow pH regime under these experimental conditions. Past synthesis studies indicate these FeOOH polymorphs are often associated and that their formation is sensitive to Fe^{III} hydrolysis rate. For example, Schwertmann et al. (1999) showed lepidocrocite forming with goethite during very slow hydrolysis Fe^{III} nitrate solutions at pH 7. In that study lepidocrocite formation became increasingly favored over goethite at slow hydrolysis rates. We attribute the occurrence of lepidocrocite at pH ~4.8 to the increase in the rate of Fe^{III} hydrolysis with increasing pH.

4.3 Effects of initial solution [SO_4] and pH on the bulk and nanoscale structure and composition of schwertmannite

Synchrotron XRD showed that schwertmannite is the only phase present in samples S1 – S5 that were formed at SO_4:Fe ratios ranging from 1 – 5 and pH ranging from ~2.4 – 3.2. The following discussion of the effects of synthesis conditions on schwertmannite crystallinity and composition both at the bulk and nanoscale is organized around these fundamental questions: (1) Does synthetic schwertmannite crystallinity change as a function of synthesis pH or initial sulfate concentration, (2) Do the amounts of sulfate and structural water in synthetic schwertmannite vary systematically with synthesis conditions, and (3) How does bulk composition of our synthetic schwertmannite compare to previous reports and what does this suggest about the composition/mineralogy of these other samples?

Does synthetic schwertmannite crystallinity change as a function of synthesis pH or initial sulfate concentration?

Schwertmannite does not have long-range structural order based on the absence of sharp diffraction peaks in powder XRD data for both natural and synthetic samples. The weak, broad XRD peaks suggest that it is poorly crystalline and nanosized; observations supported by various HR-TEM results (e.g., Loan at al., 2004; Hockridge et al., 2009; French et al., 2012, 2014). Two recent electron microscopy studies by French et al. (2012, 2014) suggest that schwertmannite is a heterogeneous mixture of sulfate-poor, partially crystalline goethite-like nanodomains (3 – 5 nm) embedded in a sulfate-rich, amorphous solid. Whether this so-called "polyphasic" characteristic of schwertmannite varies with synthesis condition, as well as how this relates to differences in

schwertmannite bulk composition are not known. Thus, we hypothesized that schwertmannite crystallinity would increase with pH due to an increase in the formation of the goethite (FeOOH)-like component. In addition, we predicted that increasing initial solution [SO_4] concentration would favor formation of the sulfate-rich, amorphous phase and decrease the FeOOH-like component.

We predicted that schwertmannite bulk crystallinity would increase with pH due to an increase in the formation of partially crystalline goethite-like nanodomains that were reported previously for schwertmannite by French et al. (2012). Synchrotron XRD analysis of S(1) through S(5) showed minimal changes in position, width and relative intensity of the characteristic 6-8 broad schwertmannite XRD peaks (**Figures 3.8 and 3.9**) as a function of pH (~2.4 - 3.2). Comparison of diffraction data for samples formed at different SO_4:Fe ratio but similar pH also shows also showed no detectable differences. This suggests that schwertmannite bulk crystallinity is not changing due to an increase in the proportion of partially crystalline goethite-like nanodomains. However, because the goethite-like nanodomains in our schwertmannite samples S(1) and S(3) have dimensions of only 3 - 5 nm, it is possible that a change in their abundance may be too small to be detected by XRD. Thus, we conclude that schwertmannite bulk crystallinity does not change significantly as a function of either initial solution [SO_4] or pH.

HR-TEM analysis of synthetic schwertmannite samples S(1) and S(3) (**Figures 3.12 and 3.13**) showed they have similar nanoscale structural heterogeneity to what has been reported previously by French et al. (2012, 2014). HR-TEM of our synthetic samples also indicate schwertmannite-like morphological characteristics, in particular the presence of needle-like features extending from the surfaces of the particles that are consistent with a "pin-cushion" or "hedge-hog" morphology. Hockridge et al. (2009) suggested that these features consist mainly of oriented goethite-like nanocrystals, and showed that they increase in size and abundance during schwertmannite aging in solution. HR-TEM images showed needle-like features increasing from just a few nanometers up to 20 – 25 nm in schwertmannite samples R1(S1) and R1(S3) (**Figures 3.12 and 3.13**). This observation suggests that the abundance and length of similar needle-like features increases with pH. However, this is not yet conclusive due to the limited number of observations made by HR-TEM in the present study.

Do the amounts of sulfate and structural water in synthetic schwertmannite vary systematically with synthesis conditions?

Oxygen (O^{2-}) and two anion groups (SO_4^{2-} and OH^-) balance the net positive charge of ferric iron (Fe^{3+}) in schwertmannite. Therefore, it is reasonable to postulate that the proportions of these different anions/anion groups in schwertmannite are somehow related. Previous studies have suggested that schwertmannite has highly variable bulk sulfate content with Fe/S molar ratios ranging from 3-15 (see Caraballo et al., 2013 for review). Yu et al. (1999) calculated that 8.5 to 8.9 water molecules per formula unit were released during the dry thermal transformation of several natural schwertmannite-bearing precipitates. However, no study to date has systematically looked at water and sulfate contents in schwertmannite as a function of synthesis conditions. Thus, we hypothesized that structural water would increase with pH due to increased formation of FeOOH in schwertmannite, and also that increasing initial solution [SO_4] during synthesis would increase bulk sulfur content in schwertmannite.

ICP-MS analyses showed that Fe/S molar ratios of approximately 4.4 to 36 are possible across the entire series of solids formed at different initial solution [SO_4] and pH conditions (Table C1 in Appendix). However, as discussed in Section 4.2, our synthesis conditions resulted in solids ranging from schwertmannite to goethite, as well as intermediate samples that are mixtures of these endmembers (and minor lepidocrocite). The samples confirmed as schwertmannite by XRD (i.e., S1 – S5) have a relatively narrow Fe/S molar ratio of 4.5 ±0.1 (**Figures 4.2 and 4.3**). This ratio is not significantly affected by either initial solution [SO_4] or pH, which suggests that the crystallinity and stoichiometry of synthetic schwertmannite is not highly variable under our synthesis conditions (discussed further below and in Section 4.4).

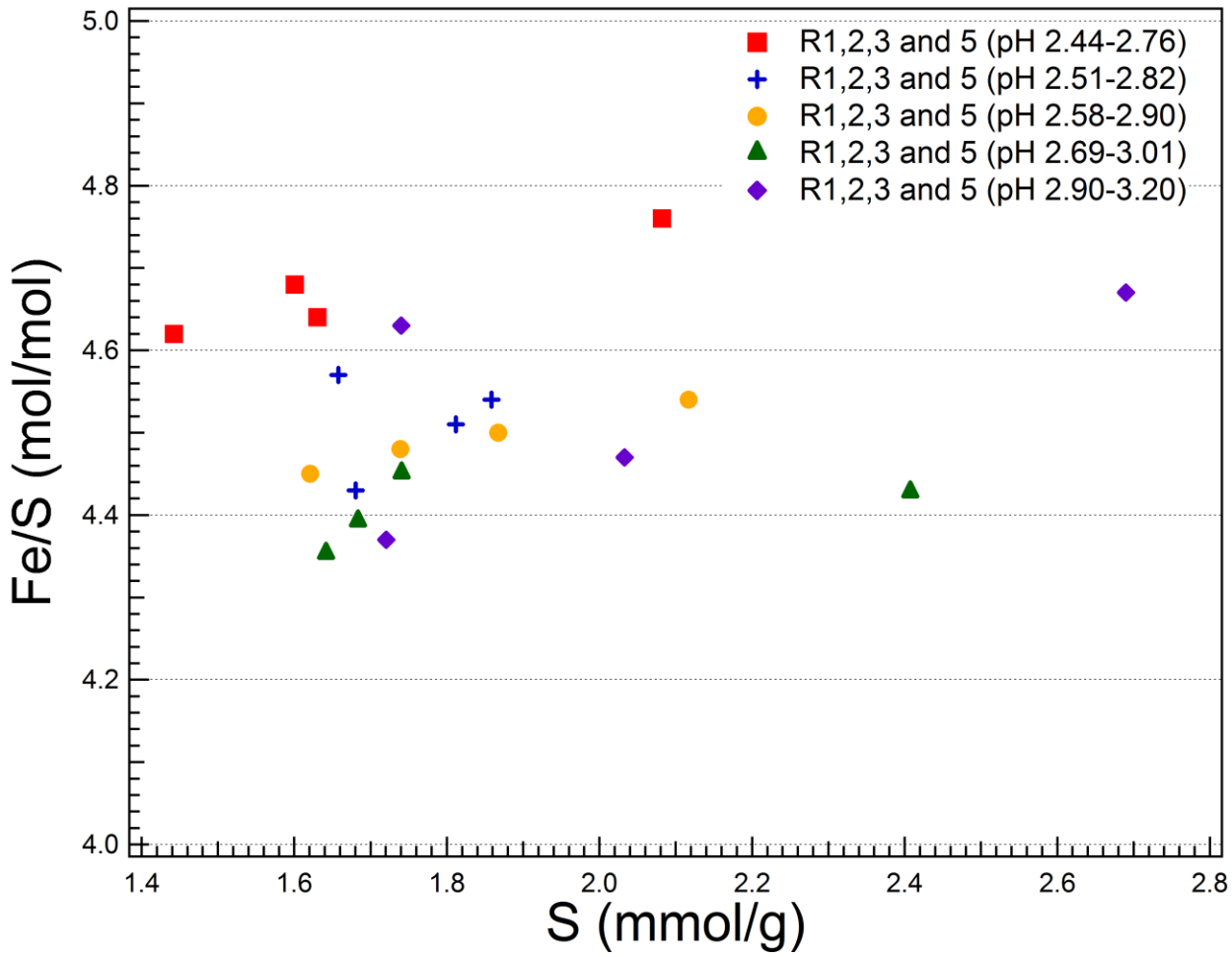

Figure 4.3. Comparison of total sulfur (S, mmol/g) to Fe/S molar ratio for 20 schwertmannite samples synthesized in this study. These data are given in Appendix C.

We predicted that water content (structural OH) would increase with synthesis pH due to an increase in the amount of partially crystalline FeOOH nanodomains in schwertmannite, and used thermal analysis to test this hypothesis. TG-DSC results showed that the T2 mass loss for schwertmannite from approximately 120 - 600 °C is primarily due to sample dehydration through removal of structural water (Figure 3.2 in Results). Comparison of T2 losses for samples R1(S1) through R1(S5), which are 17.9%, 16.9%, 19.0%, 15.2% and 15.7% (**Table 3.2**), respectively, does not show a significant trend (r^2 = 0.42). We interpret this as indicating that the amount of structural water in synthetic schwertmannite does not change with synthesis pH from ~2.4 – 3.2.

How does bulk composition of our synthetic schwertmannite compare to previous reports and what does this suggest about the composition/mineralogy of these other samples?

A comparison of the bulk composition data for our synthetic samples to data compiled by Caraballo et al. (2013) for many natural and synthetic schwertmannites (**Figure 4.4**) reveals several interesting similarities, most notably that both datasets show a dramatic increase in Fe/S ratio with decreasing total sulfur content, and that both have comparable baseline Fe/S ratios of ~4.5 at total sulfur contents of ~1.4 mmol/g and higher. However, whereas we interpret the increase in Fe/S ratio with decreasing total sulfur content in our samples as being due to goethite formation, Caraballo et al. (2013) have attributed similar behavior to changes in the bulk composition of schwertmannite. Hence, samples with low total sulfur and high Fe/S ratios in their dataset (**Figure 4.4**) would be interpreted as sulfate-poor schwertmannite. We propose two reasons for the discrepancy between these interpretations: 1) that the samples with high Fe/S ratios compiled by Caraballo et al. contain varying amounts of goethite and/or lepidocrocite that was not detected, possibly due to poor crystallinity, and 2) that our synthesis method resulted in a gap in samples in the region that would otherwise have contained the relatively sulfate-poor schwertmannites.

Composition data for the entire series of synthetic samples show a rapid increase in the Fe/S molar ratio with decreasing total sulfur content (**Figure 4.2**). XRD analysis shows that this overall trend is due to an abrupt increase in the amount of Fe-hydroxide (goethite and lepidocrocite) and corresponding decrease in the amount of schwertmannite at pH ~4 and higher (**Figure 4.4**). It is interesting to note that samples S(6), which contain minor amounts of goethite detectable by synchrotron XRD (**Figures 3.8 and 3.9**), have bulk compositions (Fe/S ratio and total sulfur) nearly identical to pure schwertmannite. This suggests that our synthesis methods would not produce sulfate-poor schwertmannite in the region where the total sulfur content would be between 1.5 and 0.4. Thus, we predict that synthesizing additional samples in this region would contain varying amounts of schwertmannite and goethite.

It is not possible to say without further characterization whether some of the samples interpreted as being sulfate-poor schwertmannite in the dataset compiled by Caraballo et al. actually contained minor Fe-hydroxide phase(s). Minor amounts (e.g., <10 wt.%) goethite and/or lepidocrocite would be difficult to detect by XRD, in particular if these phases are nanosized and partially crystalline. Thus, we are not able to say conclusively that sulfate-poor schwertmannite does not exist.

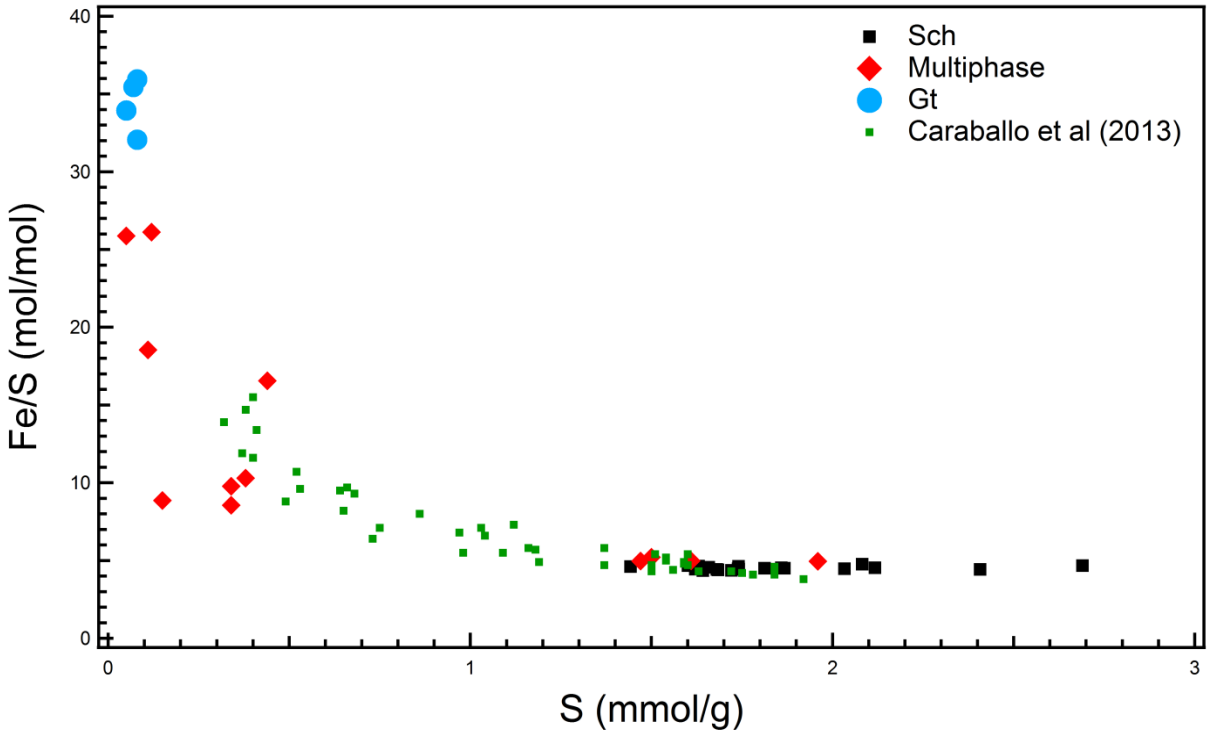

Figure 4.4. Combined ICP-MS and XRD results for samples R1, R2, R3 and R5 (S1-S9) compared to data reported by Caraballo et al. (2013). These data are given in Appendix C.

4.4 Implications of results on the schwertmannite chemical formula

Schwertmannite has the ideal formula $Fe_8O_8(OH)_6SO_4 \cdot nH_2O$, which implies a Fe/S molar ratio of 8. However, most natural and laboratory schwertmannites have been described using the standard formula $Fe_8O_8(OH)_{8-2x}(SO_4)_x$ ($1 \leq x \leq 1.75$) due to variable sulfate contents that result in Fe/S molar ratio ranging from 8 to 4.6 (Bigham et al. 1996). Caraballo et al. (2013) recently proposed that Fe/S molar ratios for schwertmannite range from 3 – 15 based on a larger collection of natural schwertmannite samples. The extremes of this range result in schwertmannite calculated formulas $Fe_8O_8(OH)_{2.6}(SO_4)_{2.7}$ and $Fe_8O_8(OH)_{6.94}(SO_4)_{0.53}$, respectively. Here, in a manner consistent with many previous schwertmannite studies, we consider the ICP-MS results for our synthetic schwertmannite in terms of the standard schwertmannite formula. Then, we propose a new, more complete schwertmannite formula based on hydroxide and sulfate contents that were independently measured by thermal analysis.

The stoichiometries of the 20 synthetic schwertmannite samples in this study are shown in **Table 4.2** based on the standard formula. The calculated molar fraction of sulfate, *x*, is between 1.68 - 1.83 mol. This is approximately at the upper limit (1.75) of the range typically reported for

schwertmannite. Plotting *x* versus log H_2SO_4 shows the effects of varying initial solution [SO_4] and pH on schwertmannite stoichiometry (**Figure 4.6**). As shown, there is an overall increase in *x* from samples S1 through S3 at the different initial solution SO_4:Fe ratios of 1, 2, 3 and 5, which eventually levels off at a maximum x = ~1.82 for the S4 and S5 samples. The overall increase in *x* corresponds with pH increasing from approximately 2.4 to 3. As shown in **Figure 4.5**, *x* decreases in samples S1, S2 and S3 as SO_4:Fe ratio increases from 1 to 5 due to a greater amount of solution [OH] in SO_4:Fe ratio 3 and 5. Although this suggests that *x* decreases with initial solution [SO_4], this trend may simply be a pH effect since the synthesis solution becomes more basic with increasing SO_4:Fe ratio (**Table 4.2**).

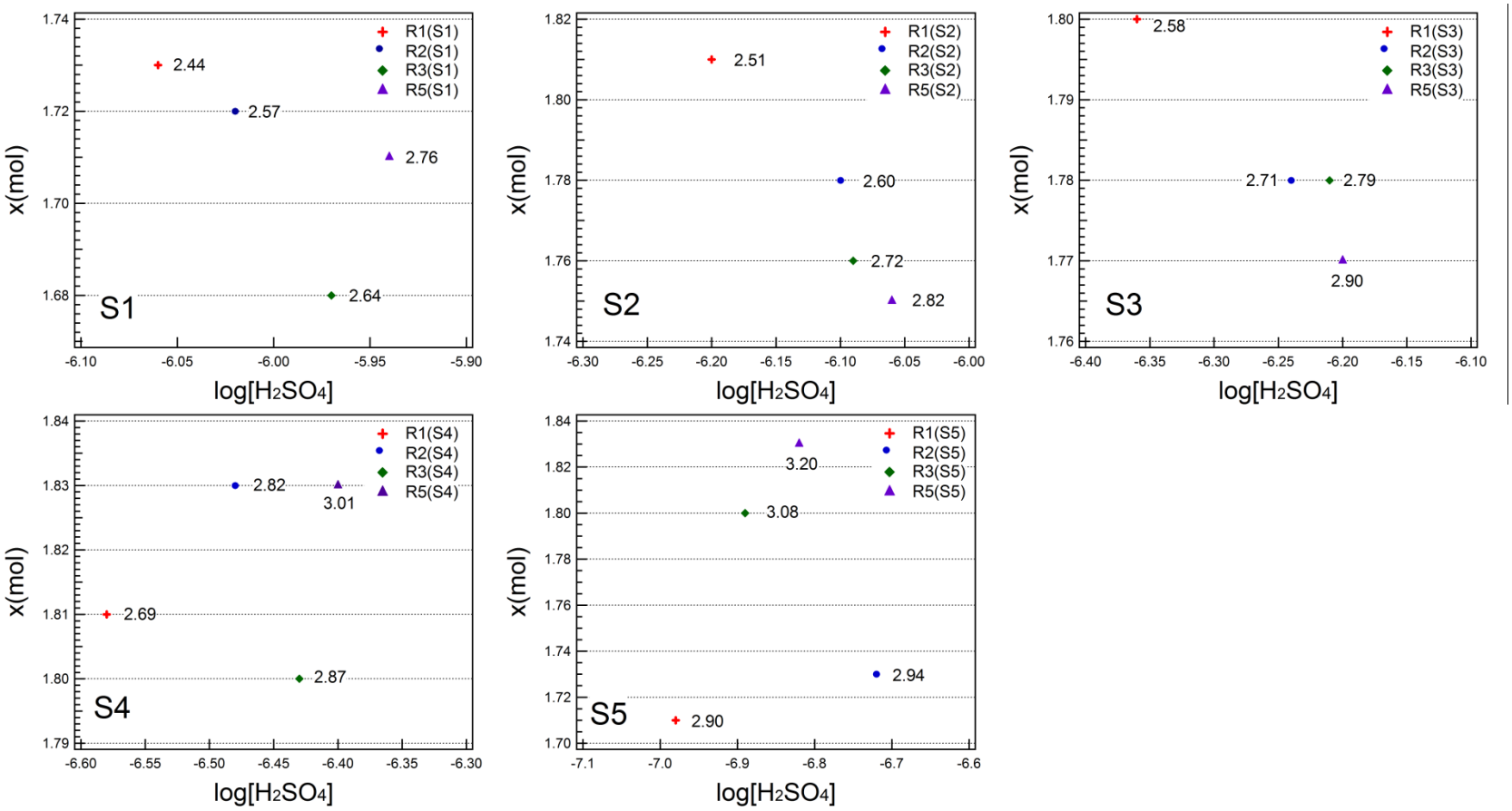

Figure 4.5. Comparison of log [H_2SO_4] to molar fraction, *x*, sulfate for 20 schwertmannite samples synthetized in this study. Numbers next to individual symbols represent the solution pH.

The overall trend in *x* (**Figure 4.6**) suggests that under these experimental conditions, there is an optimal pH range at which maximum uptake of sulfate by schwertmannite will occur. Within this optimal range, the uptake does not appear to depend appreciably on initial solution [SO_4]. We attribute the maximum in sulfate uptake in synthetic schwertmannite to the competition between solution OH and SO_4 species in terms of Fe complexation.

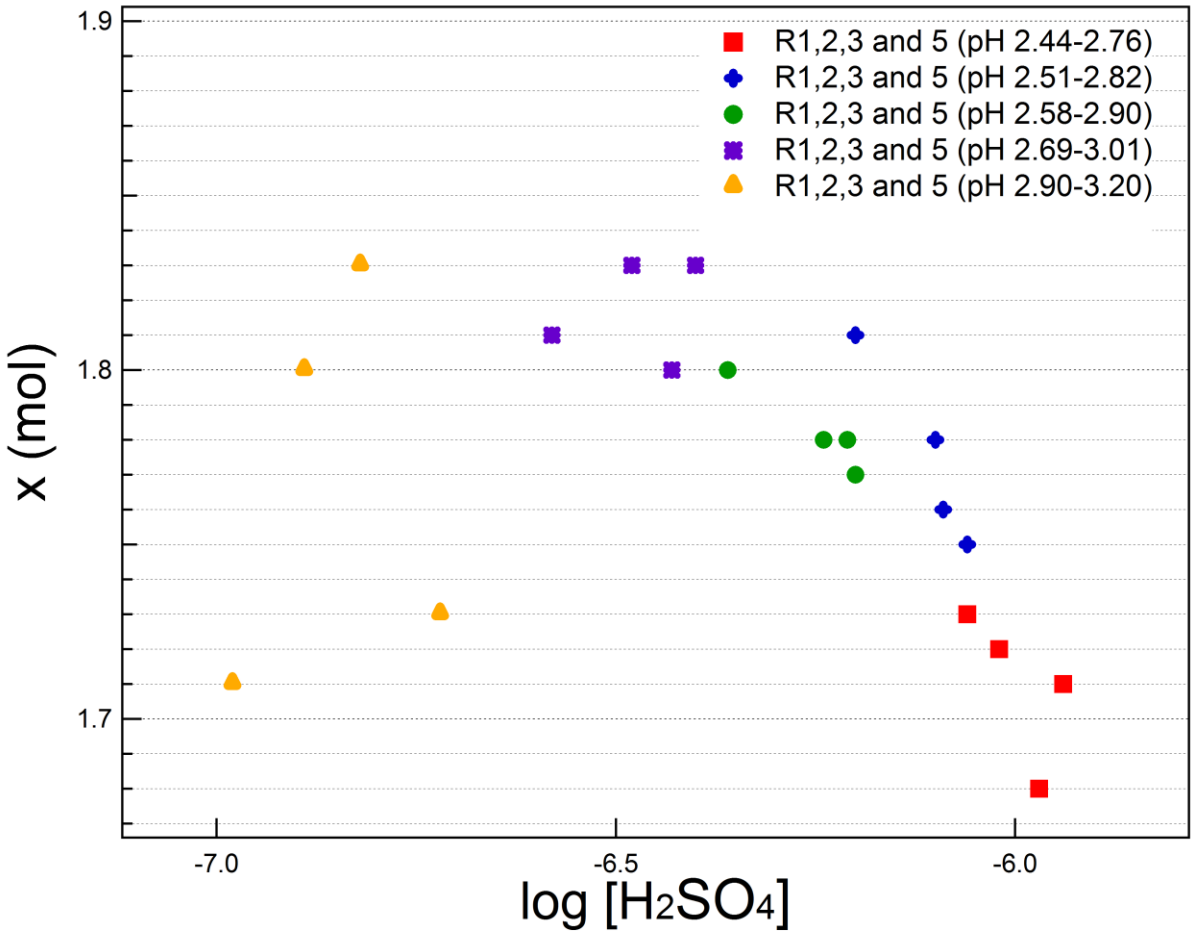

Figure 4.6. Comparison of log [H_2SO_4] to molar fraction, *x*, sulfate for 20 schwertmannite samples synthetized in this study.

Table 4.2. Stoichiometries of schwertmannite based on the $Fe_8O_8(OH)_{8-2X}(SO_4)_x$ formula measured from ICP-MS analyses.

Sample ID	Sample Type	pH	x SO_4	8-2x OH
R1(S1)	Synthetic	2.44	1.73	4.54
R1(S2)	Synthetic	2.51	1.81	4.38
R1(S3)	Synthetic	2.58	1.80	4.40
R1(S4)	Synthetic	2.69	1.81	4.38
R1(S5)	Synthetic	2.90	1.71	4.58
R2(S1)	Synthetic	2.57	1.72	4.56
R2(S2)	Synthetic	2.60	1.78	4.44
R2(S3)	Synthetic	2.71	1.78	4.44
R2(S4)	Synthetic	2.82	1.83	4.34
R2(S5)	Synthetic	2.94	1.73	4.54
R3(S1)	Synthetic	2.64	1.68	4.64
R3(S2)	Synthetic	2.72	1.76	4.48
R3(S3)	Synthetic	2.79	1.78	4.44
R3(S4)	Synthetic	2.87	1.80	4.40
R3(S5)	Synthetic	3.08	1.80	4.40
R5(S1)	Synthetic	2.76	1.71	4.58
R5(S2)	Synthetic	2.82	1.75	4.50
R5(S3)	Synthetic	2.90	1.77	4.46
R5(S4)	Synthetic	3.01	1.83	4.34
R5(S5)	Synthetic	3.20	1.83	4.34
Spain (OA)	Natural	2.40	1.97	4.06
Spain (OTSR2)	Natural	2.45	1.57	4.86
Spain (OE)	Natural	2.51	1.55	4.90
Spain (OTSR1)	Natural	2.53	1.64	4.72
Spain (OC)	Natural	2.66	1.70	4.60
Spain (O5O)	Natural	2.90	1.60	4.80
Spain (TCT2)	Natural	3.71	1.37	5.26
Spain (TCT1)	Natural	4.71	1.49	5.02

The standard formula shows that the sulfate content of our synthetic samples is less variable than natural schwertmannite. **Table 4.2** compares *x* of a subset of natural schwertmannite samples presented by Caraballo et al. (2013) to the synthetic schwertmannite samples in this study. As shown, *x* of the natural samples varies from 1.37 - 1.97 compared with 1.68 - 1.83 for the synthetic samples, which suggests that some natural schwertmannites can be relatively enriched or depleted in sulfate. As discussed in Sections 4.2 and 4.3, the sulfur-deficient samples could be an indication that they are actually mixtures of schwertmannite and Fe-hydroxides such as goethite or lepidocrocite. Alternatively, as natural schwertmannites are formed under relatively complex chemical conditions

compared with our synthetic samples, the sulfur deficiency could indicate that part of the sulfate was substituted by anions such as arsenate, selenate or nitrate (Waychunas et al., 1995).

The standard formula requires determining only the iron and sulfur concentrations in schwertmannite, which is straightforward using bulk chemical analysis methods (e.g., ICP-MS). However, of the three oxide components (Fe_2O_3, SO_3 and H_2O) in schwertmannite ICP-MS can determine only two (Fe_2O_3 and SO_3), and most studies do not explicitly accounted for water. Thus, the standard formula assumes that the amount of water, or [OH], in schwertmannite is dependent only on [SO_4] concentration; to our knowledge, no previous study has explored the validity of this assumption. Here, we used thermal analysis results to determine if the amount of water in our synthetic schwertmannite samples is consistent with the water content assumed by the standard formula.

Thermal analysis results presented in **Table 3.2** show that removal of structural water and sulfate from schwertmannite samples R1(S1 – S5) resulted in an average weight losses of 16.9 ±1.6% and 12 ±2.2%, respectively. In order to use thermal analysis data to describe schwertmannite stoichiometry, we present a new, more accurate chemical formula:

$$Fe_8O_z(OH)_{24-2z-2x}(SO_4)_x \qquad \text{Eq. 1}$$

As shown in Eq. 1, the total positive charge for eight iron atoms of 24 in the chemical formula is balanced by the total negative charge contributed by $x(SO_4)$ and y(OH). The remaining positive charge is balanced by varying the molar fraction of oxygen z(O). Calculated values of x, y, and z are given in **Table 4.3**. The average values for y and x are 8.40 ±0.94 and 1.28 ±0.14 moles, respectively, for R1(S1-S5), and 7.76 ±1.48 and 0.81 ±0.12, respectively, for R5(S1-S5). Completing charge balancing by varying the molar fraction of oxygen gives average z values of 6.51 ±0.48 and 7.31 ±0.82 moles for R1(S1-S5) and R5(S1-S5), respectively. Interestingly, in all cases except for R5(S2) the z values are less than 8, which is the molar fraction assumed in the standard chemical formula. Discussed further below, this may suggest fewer "bridging" oxygens (i.e., Fe-O-Fe) in the schwertmannite structure than previously thought. The comparable averages for x, y, and z in samples R1(S1-S5) and R1(S1-S5) indicate that schwertmannite stoichiometry is not strongly correlated with initial solution [SO_4] or pH.

As shown in **Table 4.3**, the more complete formula has calculated *z* values ranging from 3.47 - 5.76 when applied to data reported previously for natural schwertmannites (Bigham and Nordstrom, 2000). Why natural samples show lower oxygen content than our synthetic samples is not entirely clear at present, but may be related to degree of crystallinity and the amount of bridging oxygens in the structure. Lower crystallinity is expected for natural schwertmannite due to their formation in the presence of natural organics or other species that inhibit crystallization. The average values for *y* and *x* are 11.76 ±1.43 and 1.48 ±0.19, respectively, do not appear to have a statistically significant difference from synthetic schwertmannite samples R1(S1-S5) and R5(S1-S5) in this study. This tells us that our systematic variation of synthesis conditions combined with the systematic application of different characterization methods is an accurate portrayal of natural schwertmannite.

Table 4.3. Stoichiometries of schwertmannite based on the $Fe_8O_z(OH)_{24-2z-2x}(SO_4)_x$ formula from thermal analysis.

Sample ID	Sample Type	pH	x SO_4	y OH	z O
R1(S1)	Synthetic	2.44	1.21	8.89	6.34
R1(S2)	Synthetic	2.51	1.08	8.17	6.84
R1(S3)	Synthetic	2.58	1.37	9.76	5.74
R1(S4)	Synthetic	2.69	1.37	7.44	6.90
R1(S5)	Synthetic	2.90	1.39	7.73	6.74
Average R1(S1-S5)	Synthetic		1.28	8.40	6.51
STD %			0.14	0.94	0.48
R5(S1)	Synthetic	2.76	0.95	8.00	7.05
R5(S2)	Synthetic	2.82	0.68	6.23	8.20
R5(S3)	Synthetic	2.90	0.90	10.15	6.03
R5(S4)	Synthetic	3.01	0.82	7.03	7.67
R5(S5)	Synthetic	3.20	0.69	7.38	7.62
Average R5(S1-S5)	Synthetic		0.81	7.76	7.31
STD%			0.12	1.48	0.82
PI3	Natural	2.65	1.74	10.92	4.80
Z5106	Synthetic	2.90	1.67	13.72	3.47
Nb-1	Natural	3.0	1.59	11.13	4.84
DP4226	Natural	3.0	1.38		
MG1118	Natural	3.0	1.36		
Y3b	Natural	3.10	1.19	10.11	5.76
La-1	Natural	3.10	1.50	10.48	5.26
Py-4	Natural	3.20	1.62	13.10	3.82
B-2000s	Synthetic		1.24	12.88	4.32
*Average reported data			1.48	11.76	4.61
STD%			0.19	1.43	0.80

*Reference data from Bigham and Nordstrom (2000)

In order to more accurately mimic natural environments, future synthesis conditions may need to consider other initial solution factors that lead to solid schwertmannite formation. Some factors may include but are not limited to the type of oxidizing agent, different concentrations of initial sulfate or oxidizing agent, the length of time the solution will stir and age at static conditions, whether heating is added to the solution, or whether precipitates are air dried, freeze dried or dried with heat. Varying synthesis conditions are to be expected from experiment to experiment, yet the overall approach should be to form schwertmannite precipitates similar to the composition and structure of natural samples.

5. CONCLUSIONS AND OUTLOOK

We have used systematically varied synthesis conditions and the systematic application of complementary analytical characterization methods to examine to what extent varying initial solution chemistry, specifically initial solution sulfate concentration and pH, affected the composition and crystallinity of schwertmannite and other synthesis products. Mineralogical characterization by synchrotron XRD showed that the synthesis products ranged from predominantly schwertmannite at lower pH (~2.4 – 3.2) to goethite and, sometimes, minor lepidocrocite at higher pH (~4 - 5.6). Increasing the initial solution [SO_4] from 72 to 360 mM had no discernable effect on the overall mineralogy. Bulk chemical analysis by ICP-MS showed that the samples became increasingly sulfate deficient above pH ~4, which corresponded with the abrupt increase in crystallinity and in the formation of the Fe-hydroxides. Scanning electron microscopy established the morphological and size characteristics of goethite nanocrystals and schwertmannite aggregates. Consistent with prior studies, high-resolution TEM showed that our synthetic schwertmannite consists of a mixture of partially crystalline goethite-like nanodomains (3 – 5 nm) and an amorphous solid. Finally, thermal analysis showed three stages of weight loss in the samples with increasing temperature corresponding with removal of loosely bound water, structural water, and sulfate (decomposition), respectively.

We had predicted that increasing solution pH would favor the formation of a FeOOH-like component in schwertmannite, thus resulting in higher crystallinity, increased water content, and decreased sulfate content. Our results did show that increasing solution pH favored the formation of more crystalline Fe-hydroxide, mainly goethite. However, synchrotron XRD showed no detectable changes in schwertmannite crystallinity. Correspondingly, bulk Fe/S ratio and water contents of the same samples did not change significantly with pH (~2.4 – 3.2). HR-TEM analysis provided some evidence that the abundance and size of needle-like features in schwertmannite, which consisted mainly of goethite-like nanodomains, increased with pH. Although this could suggest an increase in schwertmannite crystallinity – one that could be too subtle to detect by synchrotron XRD – more studies would be needed to confirm. Using the standard schwertmannite formula ($Fe_8O_8(OH)_{8-2x}(SO_4)_x$ where $1 \leq x \leq 1.75$), we find that sulfate content (x) does increase slightly with pH but that it reaches a maximum ~1.82, a value slightly above the upper limit of 1.75 most often applied to schwertmannite.

We had also predicted that increasing initial solution sulfate concentration (i.e., SO_4:Fe molar ratio) would suppress the formation of FeOOH, thus resulting in schwertmannite with lower crystallinity (more sulfate-rich amorphous content), decreased water content, and increased sulfate content. Our results showed that increasing initial sulfate concentration by up to 5X did not suppress the formation of goethite and had virtually no effect on overall mineralogy as a function of pH. In addition, varying initial sulfate concentration did not affect schwertmannite crystallinity. The small decrease in the molar fraction of sulfate (x) with increasing solution SO_4:Fe molar ratio may indicate a minor dependence of schwertmannite composition on the initial solution sulfate concentration. However, as the pH of the samples formed at different SO_4:Fe molar ratios varied slightly, it was not possible to determine if this effect was separate from the pH effect. Thus, we conclude that schwertmannite crystallinity and composition is approximately constant with initial solution sulfate concentration and pH under our experimental conditions.

Finally, we have proposed a more accurate chemical formula, $Fe_8O_z(OH)_{24-2z-2x}(SO_4)_x$ for schwertmannite based on our use of thermal analysis to independently measure OH and SO_4 content. Stoichiometries for $x(SO_4)$ and y(OH) exhibit only small variations over pH ranging from 2.4 – 3.2. The errors on the average molar fractions (x and y) for the five samples of schwertmannite in each series are comparable to those calculated based only on Fe and S concentrations from ICP-MS using the standard formula. This validates our more complete approach of using thermal analysis to establish schwertmannite stoichiometry. Interestingly, calculating the stoichiometry using the more accurate formula results in z values less than 8, which is the molar fraction assumed in the standard chemical formula. This may suggest that there are fewer bridging (i.e., Fe-O-Fe) bonds in schwertmannite than previously thought. This finding must be considered in future work aimed at better understanding schwertmannite atomic structure.

6. FUTURE DIRECTIONS

Our work shows that the crystallinity and composition of schwertmannite formed under systematically controlled synthesis conditions are approximately constant with both initial solution sulfate concentration and pH. Findings of this research stimulate new questions regarding schwertmannite structure and composition that require further study:

1) Does sulfate-poor schwertmannite actually exist? If so, do its bulk compositional characteristics reflect an increase in the proportion of FeOOH-like nanodomains and decrease in the sulfate-rich, amorphous solid?

2) What factors other than solution chemistry (e.g., aging, oxidation rate, aqueous Fe^{2+}/Fe^{3+}, etc.) are responsible for determining schwertmannite crystallinity and composition?

3) Would schwertmannite crystallinity and composition be affected at higher SO_4:Fe molar ratios (e.g., <1 or 10 to 100) that sometimes occur in certain AMD systems?

4) What is the structure of schwertmannite?

5) What formation process leads to the nanoscale heterogeneity of schwertmannite?

7. REFERENCES

BIGHAM, J. M., CARLSON, L. & MURAD, E. 1994. Schwertmannite, a New Iron Oxyhydroxysulphate from Pyhasalmi, Finland, and Other Localities. *Mineralogical Magazine,* 58**,** 641-648.

BIGHAM, J. M. & NORDSTROM, D. K. 2000. Iron and aluminum hydroxysulfates from acid sulfate waters. *Sulfate Minerals - Crystallography, Geochemistry and Environmental Significance,* 40**,** 351-403.

BIGHAM, J. M., SCHWERTMANN, U., CARLSON, L. & MURAD, E. 1990. A Poorly Crystallized Oxyhydroxysulfate of Iron Formed by Bacterial Oxidation of Fe(Ii) in Acid-Mine Waters. *Geochimica Et Cosmochimica Acta,* 54**,** 2743-2758.

BRADY, K. S., BIGHAM, J. M., JAYNES, W. F. & LOGAN, T. J. 1986. Influence of Sulfate on Fe-Oxide Formation - Comparisons with a Stream Receiving Acid-Mine Drainage. *Clays and Clay Minerals,* 34**,** 266-274.

CARABALLO, M. A., RIMSTIDT, J. D., MACIAS, F., NIETO, J. M. & HOCHELLA, M. F. 2013. Metastability, nanocrystallinity and pseudo-solid solution effects on the understanding of schwertmannite solubility. *Chemical Geology,* 360**,** 22-31.

DAVIDSON, L. E., SHAW, S. & BENNING, L. G. 2008. The kinetics and mechanisms of schwertmannite transformation to goethite and hematite under alkaline conditions. *American Mineralogist,* 93**,** 1326-1337.

FERNANDEZ-MARTINEZ, A., TIMON, V., ROMAN-ROSS, G., CUELLO, G. J., DANIELS, J. E. & AYORA, C. 2010. The structure of schwertmannite, a nanocrystalline iron oxyhydroxysulfate. *American Mineralogist,* 95**,** 1312-1322.

FRENCH, R. A., CARABALLO, M. A., KIM, B., RIMSTIDT, J. D., MURAYAMA, M. & HOCHELLA, M. F. 2012. The enigmatic iron oxyhydroxysulfate nanomineral schwertmannite: Morphology, structure, and composition. *American Mineralogist,* 97**,** 1469-1482.

FRENCH, R. A., MONSEGUE, N., MURAYAMA, M. & HOCHELLA, M. F. 2014. The structure and transformation of the nanomineral schwertmannite: a synthetic analog representative of field samples. *Physics and Chemistry of Minerals,* 41**,** 237-246.

HAMMARSTROM, J. M., SEAL, R. R., MEIER, A. L. & KORNFELD, J. M. 2005. Secondary sulfate minerals associated with acid drainage in the eastern US: recycling of metals and acidity in surficial environments. *Chemical Geology,* 215**,** 407-431.

HOCKRIDGE, J. G., JONES, F., LOAN, M. & RICHMOND, W. R. 2009. An electron microscopy study of the crystal growth of schwertmannite needles through oriented aggregation of goethite nanocrystals. *Journal of Crystal Growth,* 311**,** 3876-3882.

JONSSON, J., PERSSON, P., SJOBERG, S. & LOVGREN, L. 2005. Schwertmannite precipitated from acid mine drainage: phase transformation, sulphate release and surface properties. *Applied Geochemistry,* 20**,** 179-191.

LOAN, M., COWLEY, J. M., HART, R. & PARKINSON, G. M. 2004. Evidence on the structure of synthetic schwertmannite. *American Mineralogist,* 89**,** 1735-1742.

MURAD, E., SCHWERTMANN, U., BIGHAM, J. M. & CARLSON, L. Mineralogical characteristics of poorly crystallized precipitates formed by oxidation of Fe super (2+) in acid sulfate waters. A. C. S. Symposium Series, 1994.

NORDSTROM, D. K. & ALPERS, C. N. 1999. Negative pH, efflorescent mineralogy, and consequences for environmental restoration at the Iron Mountain Superfund site, California. *Proceedings of the National Academy of Sciences of the United States of America,* 96**,** 3455-3462.

NORDSTROM, D. K., ALPERS, C. N., PTACEK, C. J. & BLOWES, D. W. 2000. Negative pH and extremely acidic mine waters from Iron Mountain, California. *Environmental Science & Technology,* 34**,** 254-258.

REGENSPURG, S., BRAND, A. & PEIFFER, S. 2004. Formation and stability of schwertmannite in acidic mining lakes. *Geochimica Et Cosmochimica Acta,* 68**,** 1185-1197.

REINSCH, B. C., FORSBERG, B., PENN, R. L., KIM, C. S. & LOWRY, G. V. 2010. Chemical Transformations during Aging of Zerovalent Iron Nanoparticles in the Presence of Common Groundwater Dissolved Constituents. *Environmental Science & Technology,* 44**,** 3455-3461.

YU, J. Y., PARK, M. & KIM, J. 2002. Solubilities of synthetic schwertmannite and ferrihydrite. *Geochemical Journal,* 36**,** 119-132.

APPENDIX A. SUPPLEMENTARY INFORMATION

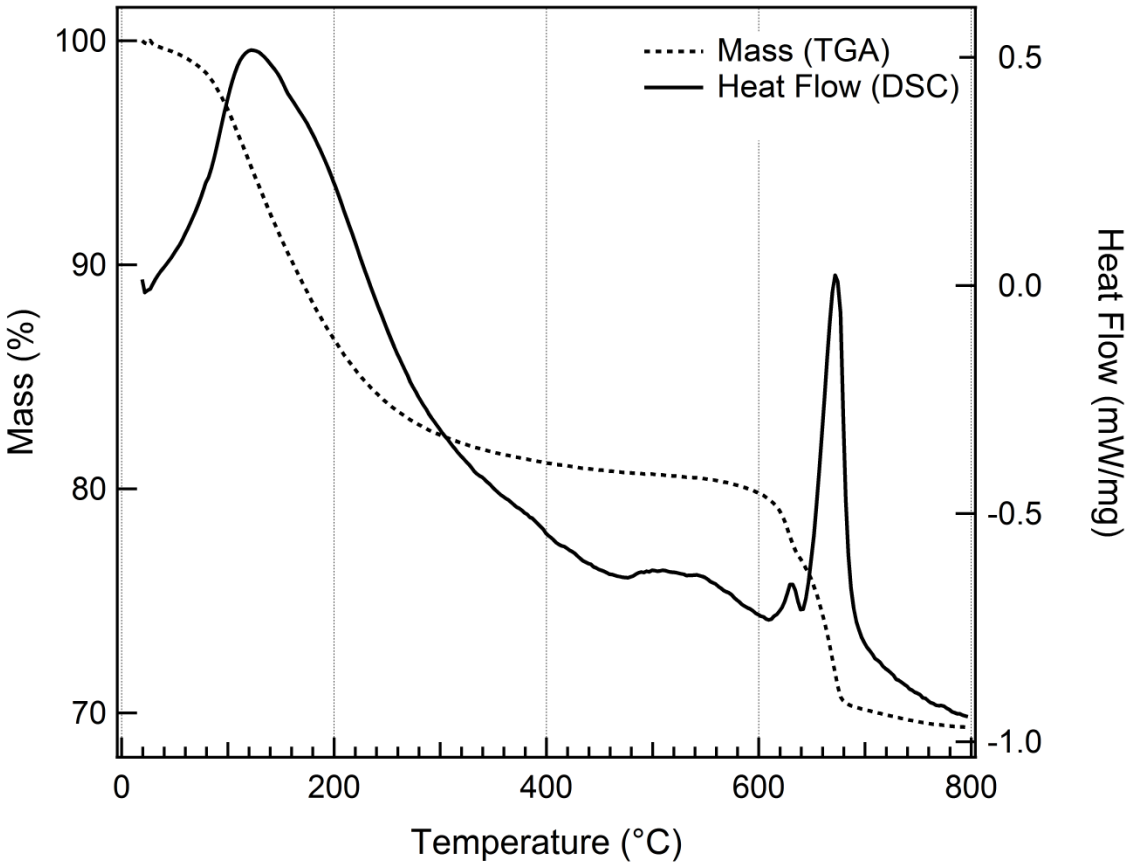

Figure A.1. TGA-DSC curve for R1(S2).

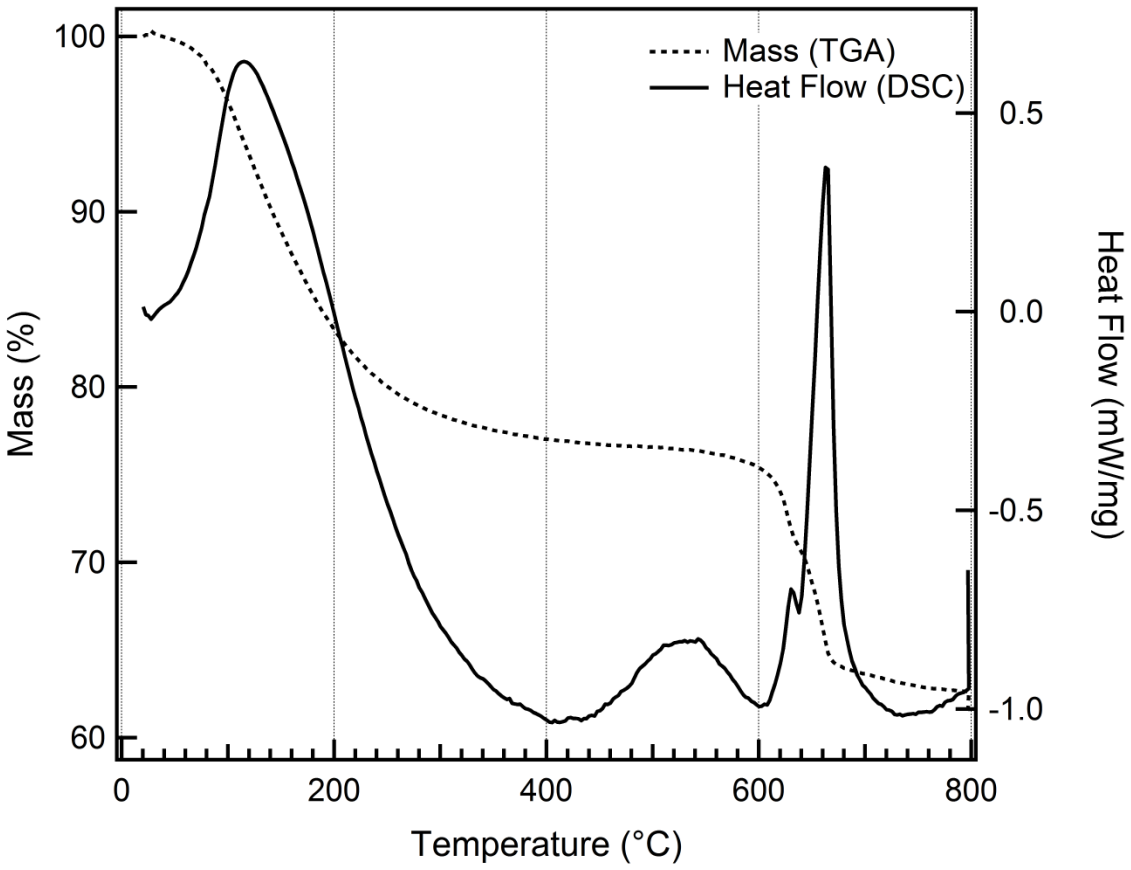

Figure A.2. TGA-DSC curve for R1(S3).

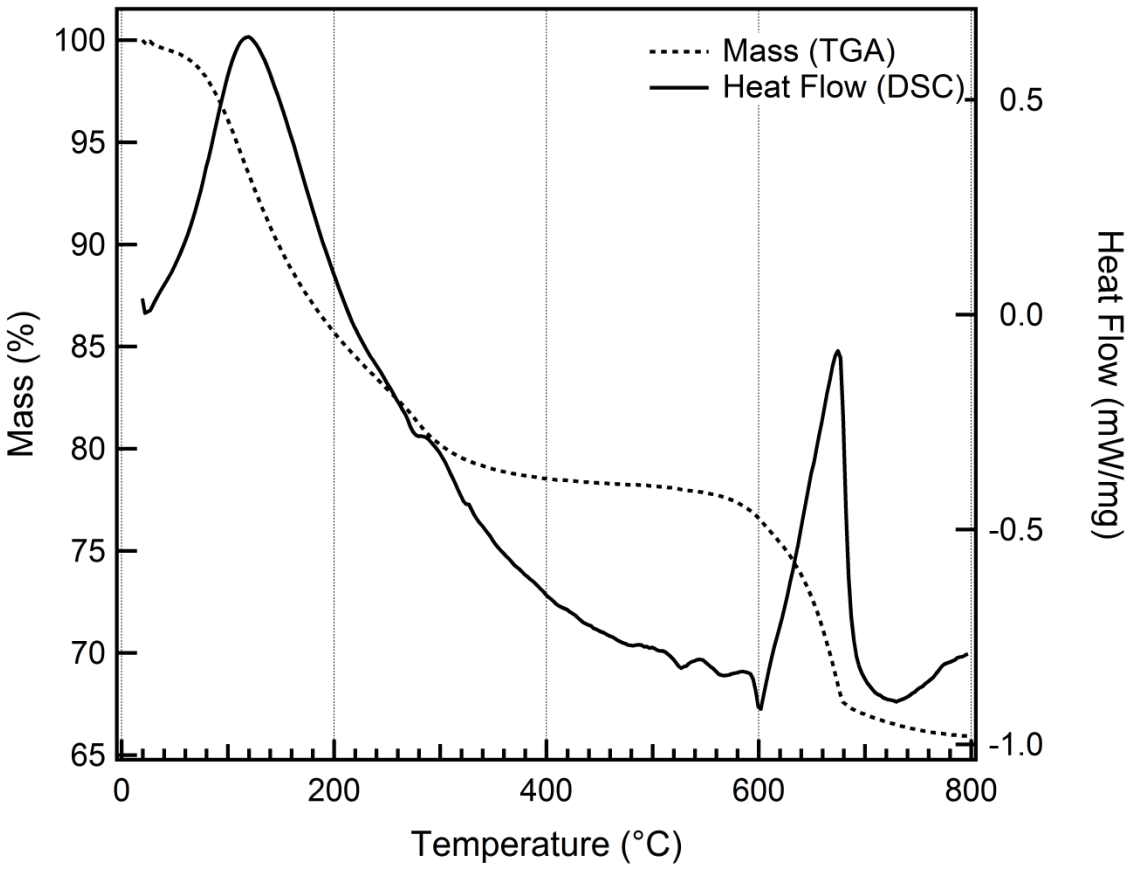

Figure A.3. TGA-DSC curve for R1(S4).

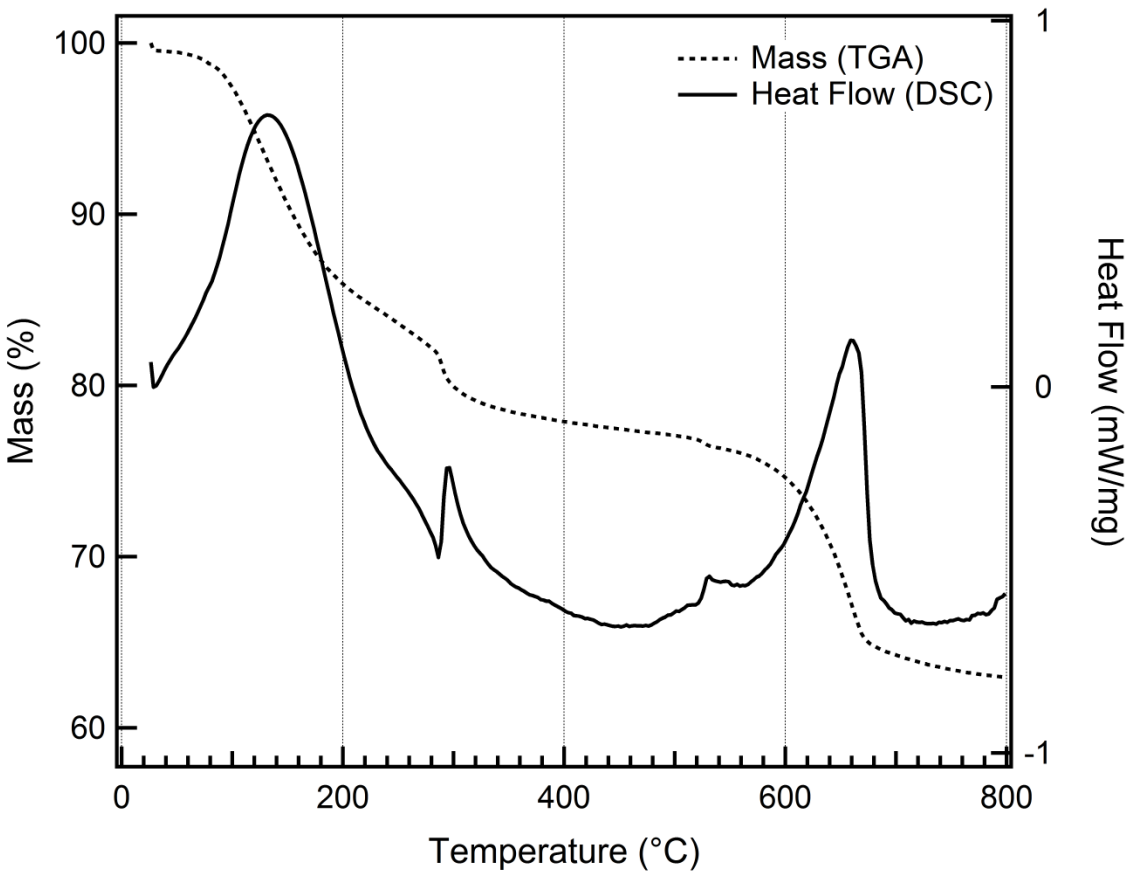

Figure A.4. TGA-DSC curve for R1(S5).

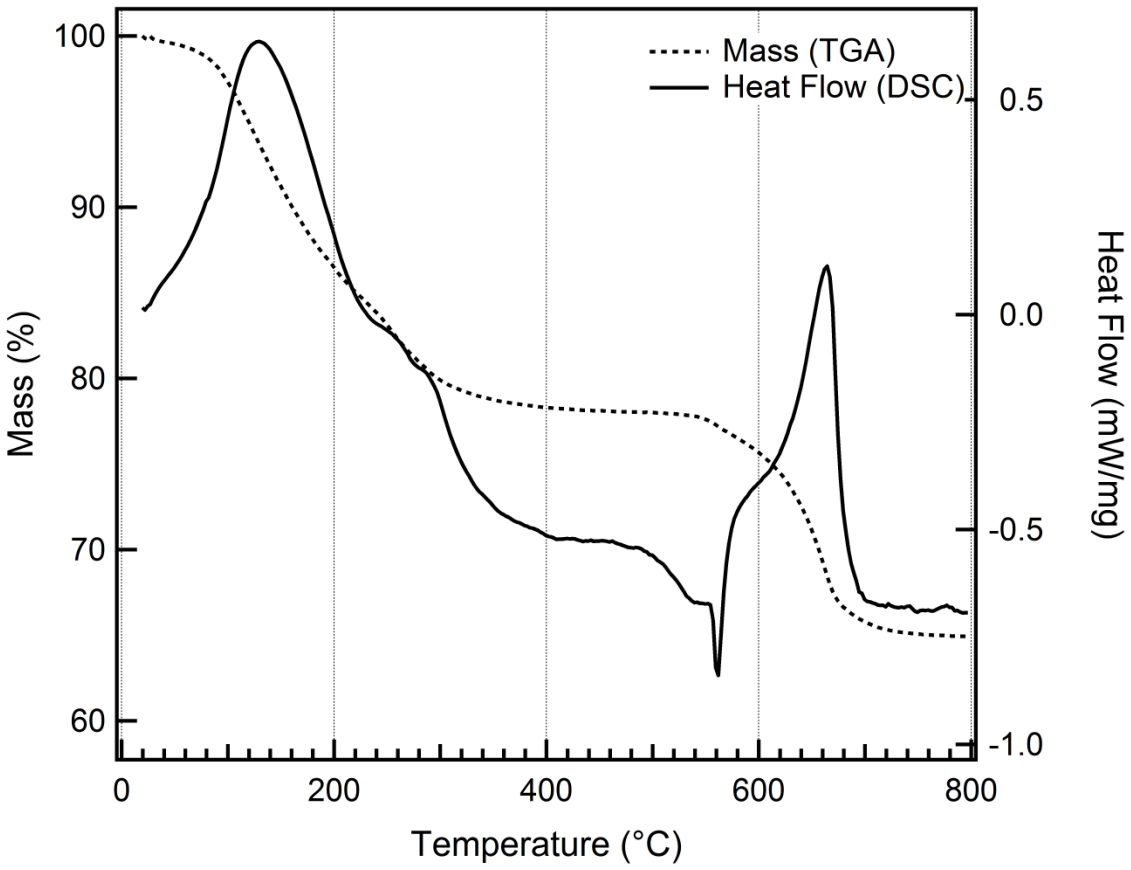

Figure A.5. TGA-DSC curve for R1(S6).

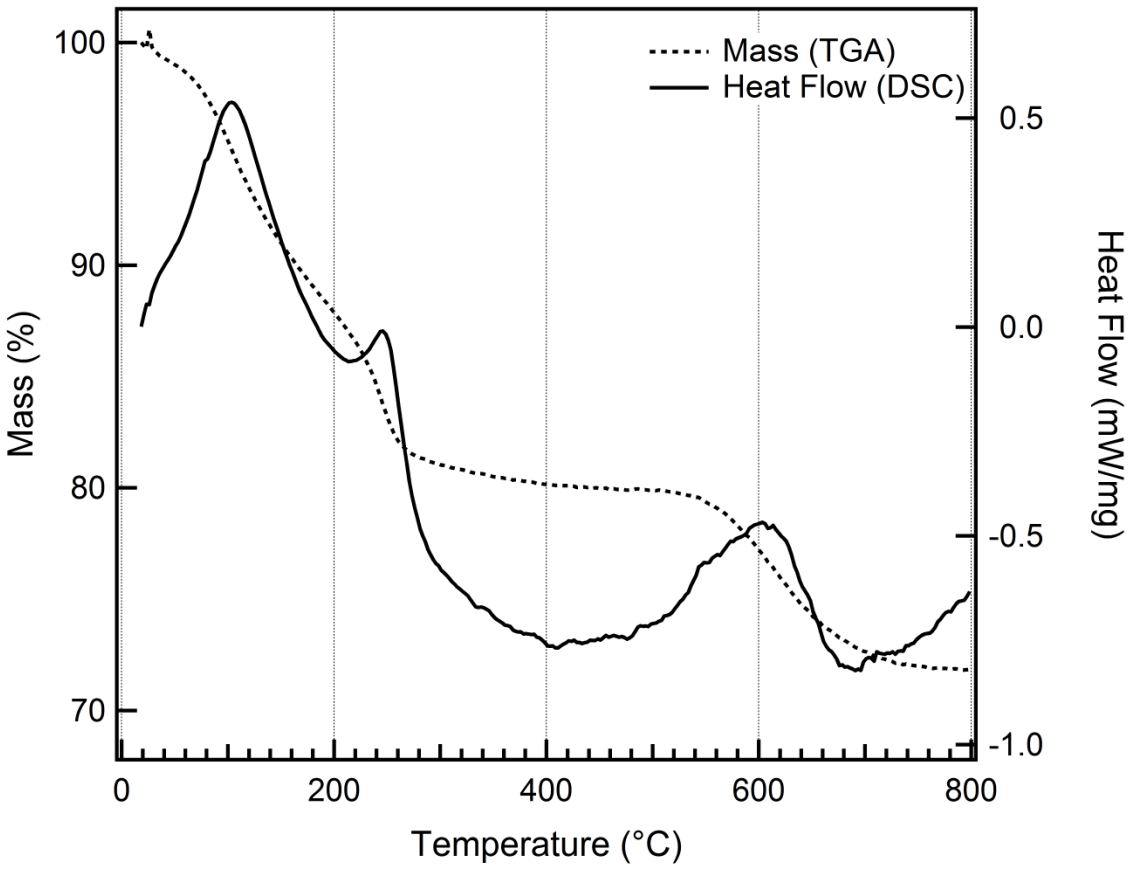

Figure A.6. TGA-DSC curve for R1(S7).

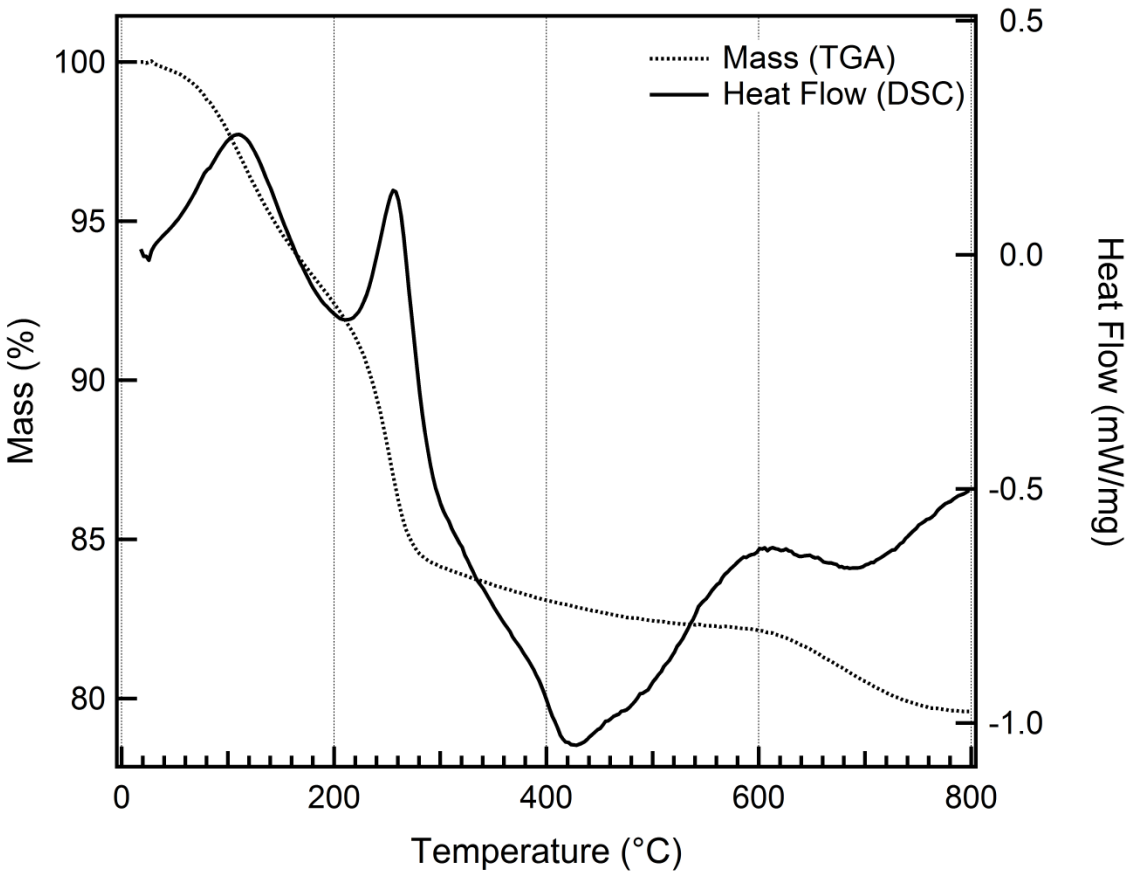

Figure A.7. TGA-DSC curve for R1(S8).

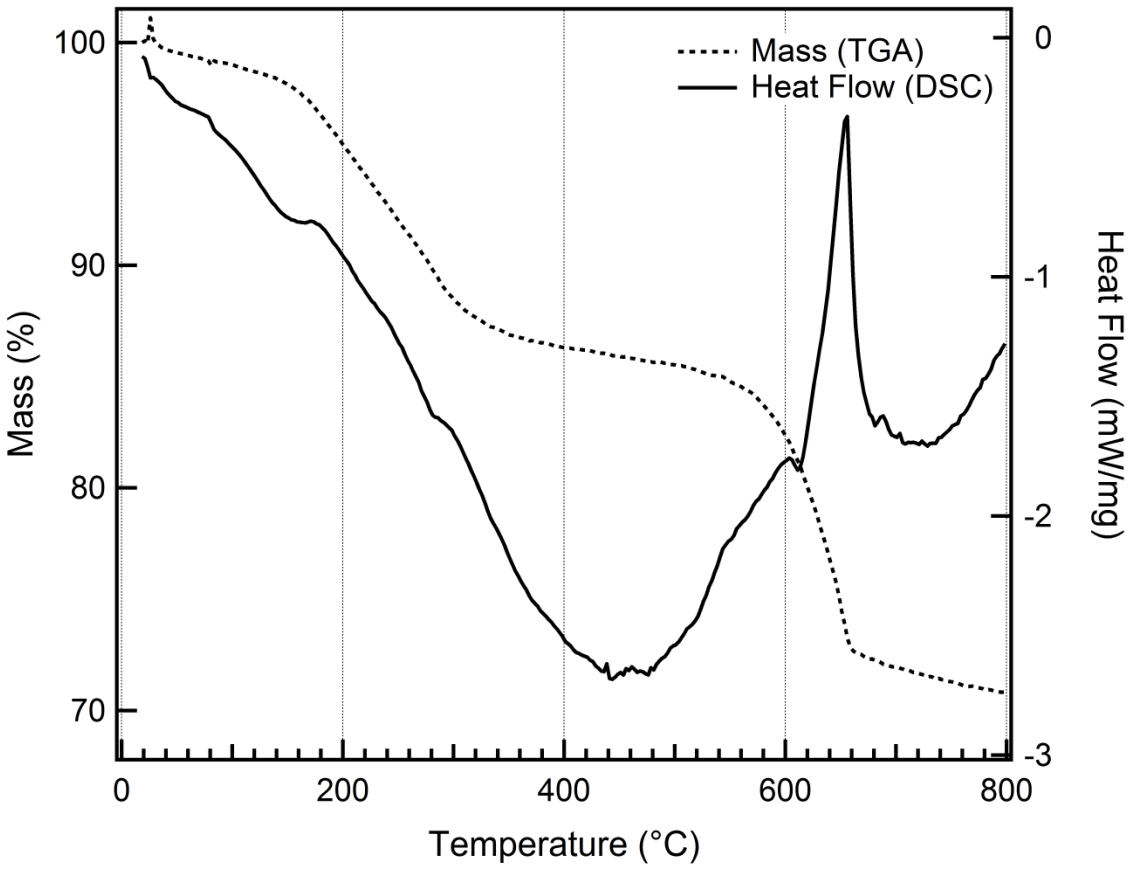

Figure A.8. TGA-DSC curve for R5(S1).

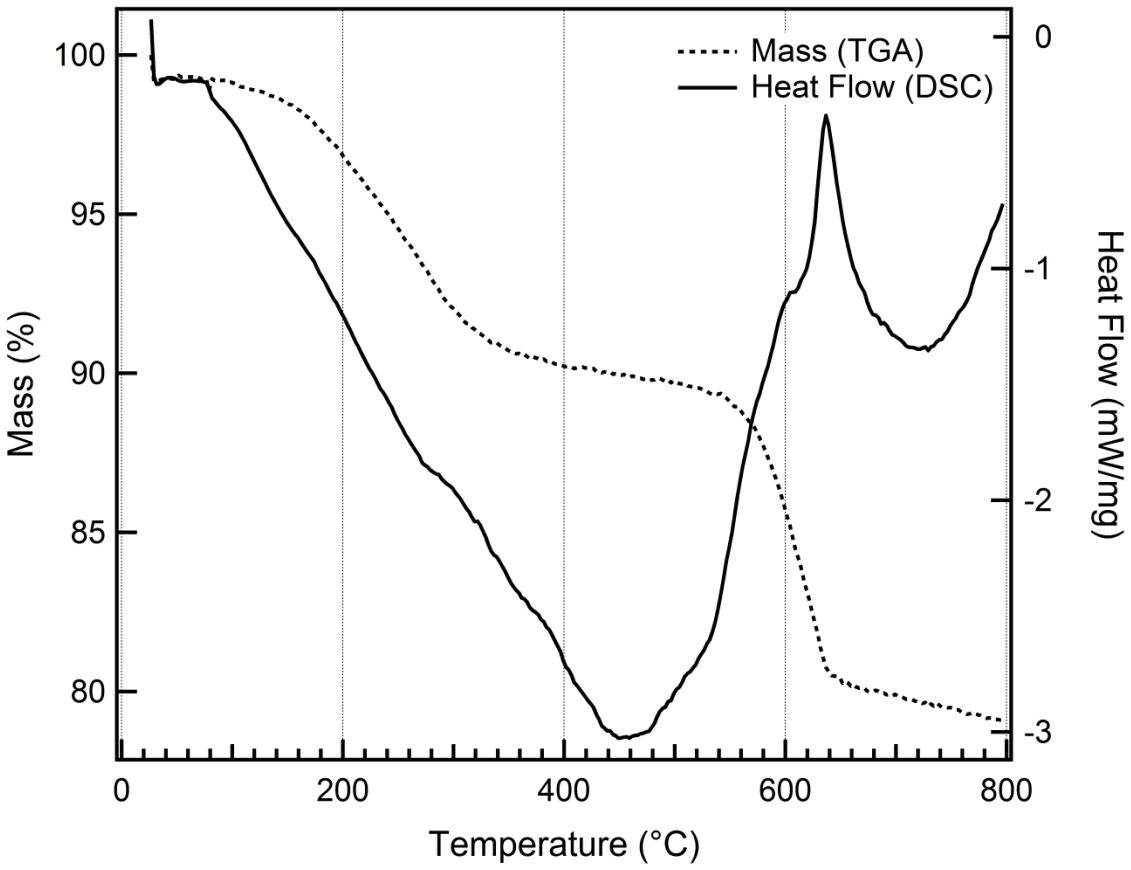

Figure A.9. TGA-DSC curve for R5(S2).

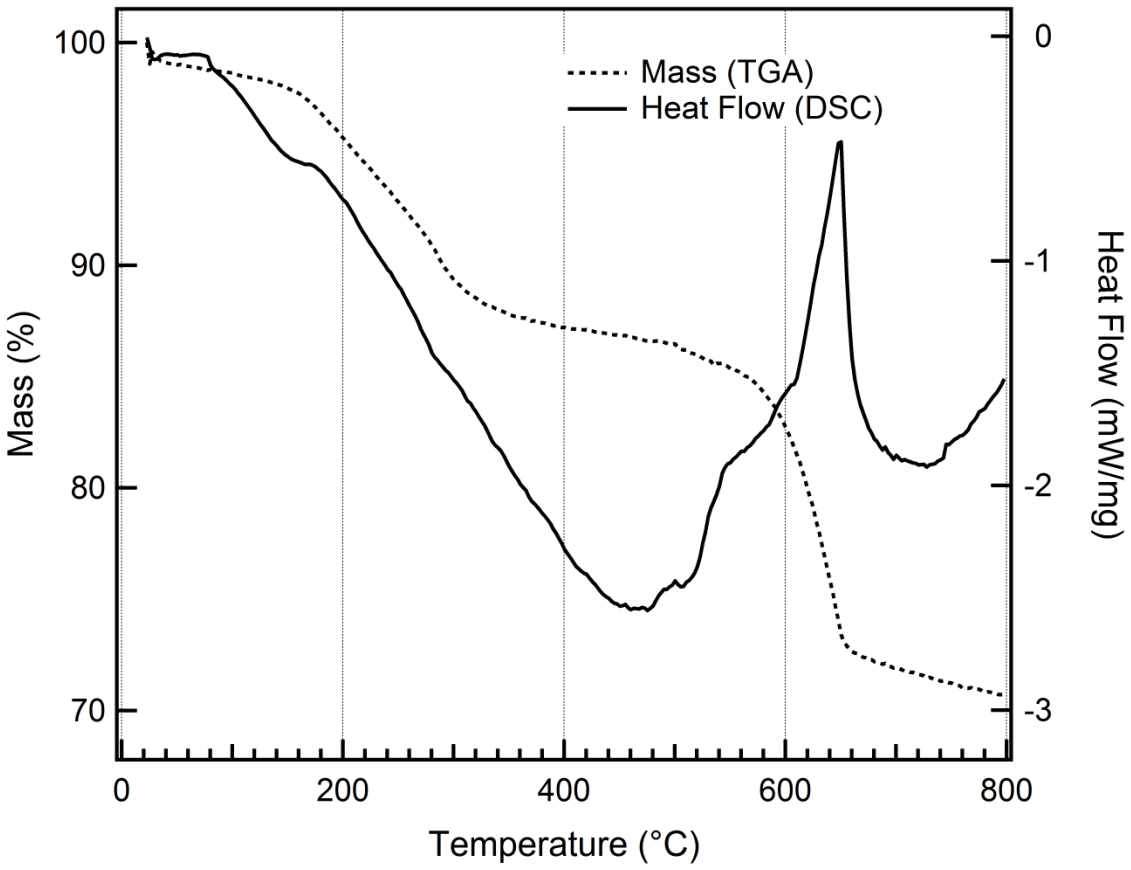

Figure A.10. TGA-DSC curve for R5(S3).

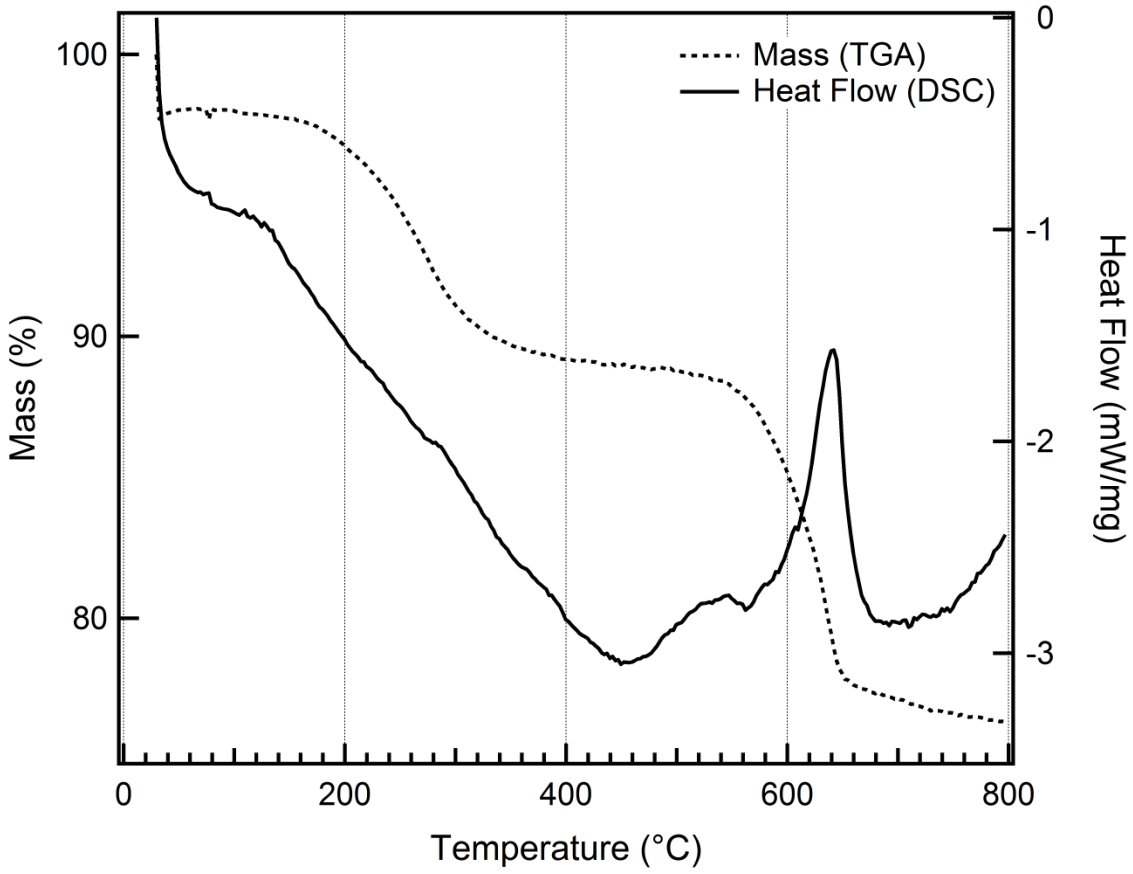

Figure A.11. TGA-DSC curve for R5(S4).

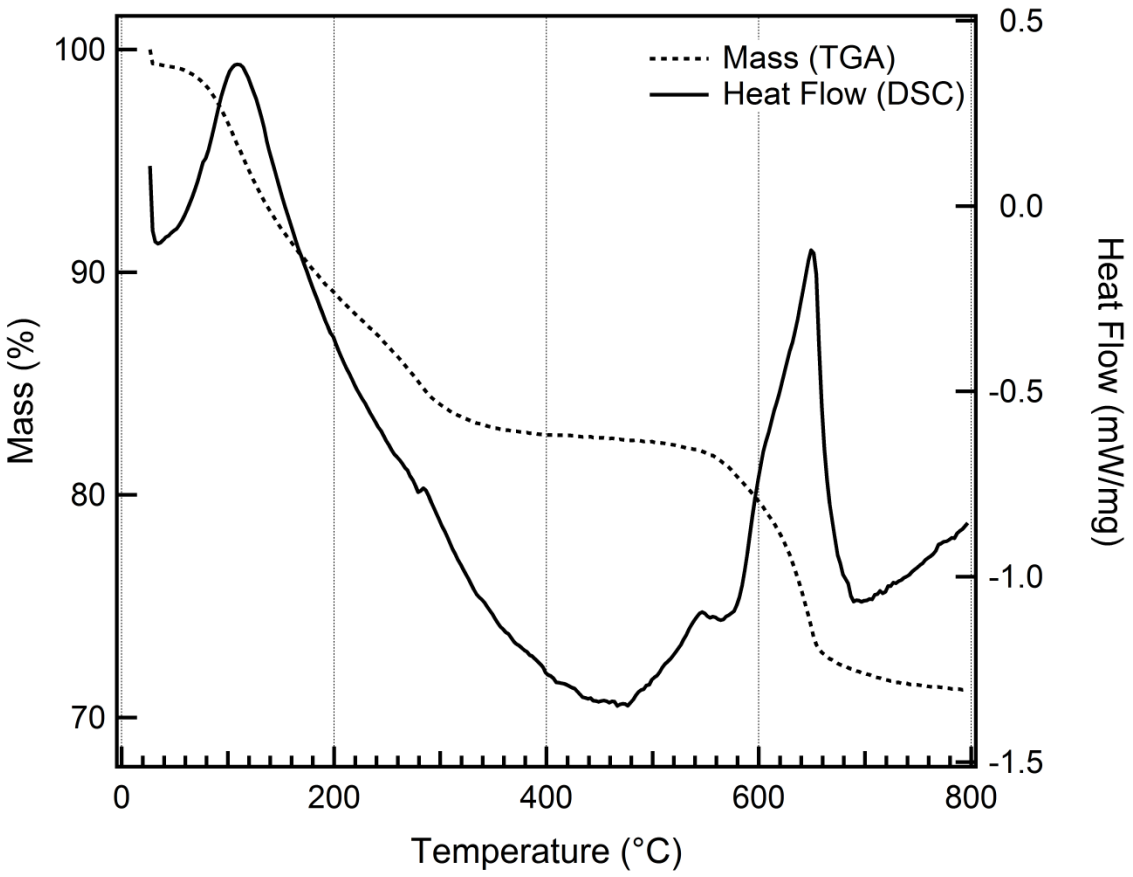

Figure A.12. TGA-DSC curve for R5(S

APPENDIX B. SUPPLEMENTARY INFORMATION

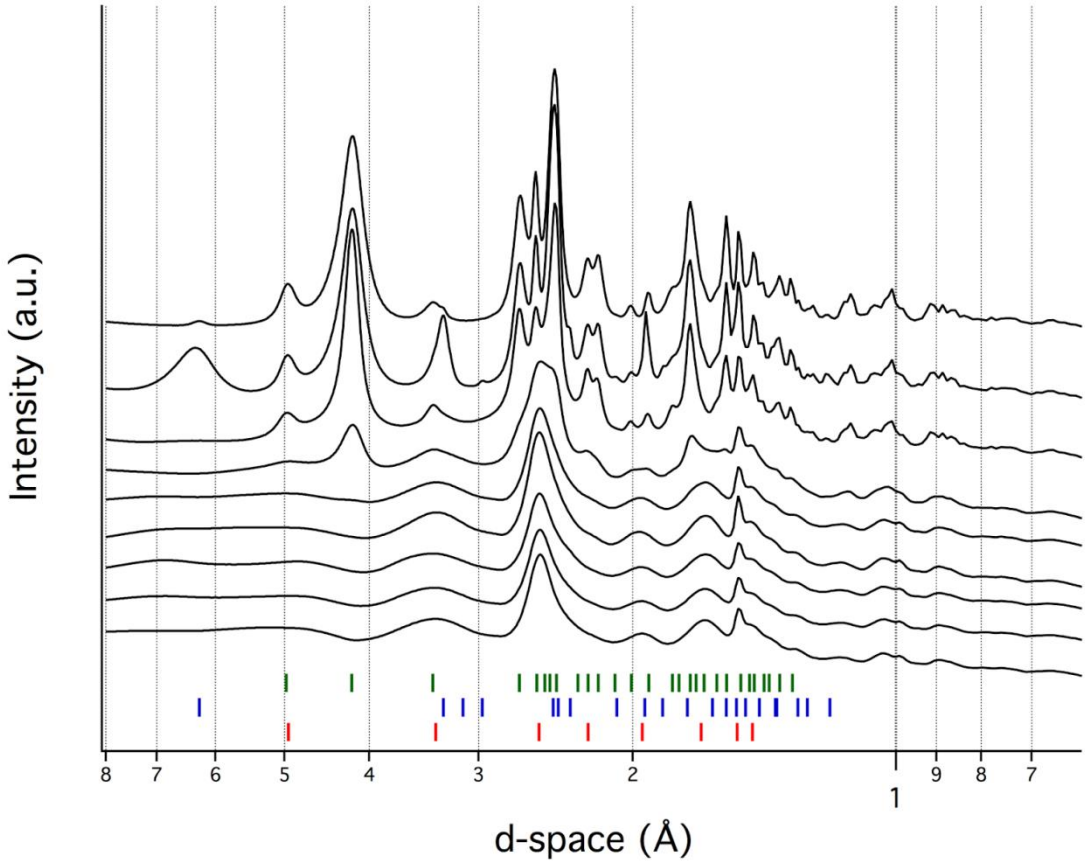

Figure B.1. Background-subtracted synchrotron powder diffraction data with intensity plotted in arbitrary units on the ordinate versus d-space in Å on the abscissa. The samples were synthesized at $[SO_4]/[Fe]=2.0$. pH increases from the bottom to the top. Lower tick marks show the calculated positions of reflections for schwertmannite (bottom, red), lepidocrocite (middle, blue) and goethite (top,green).

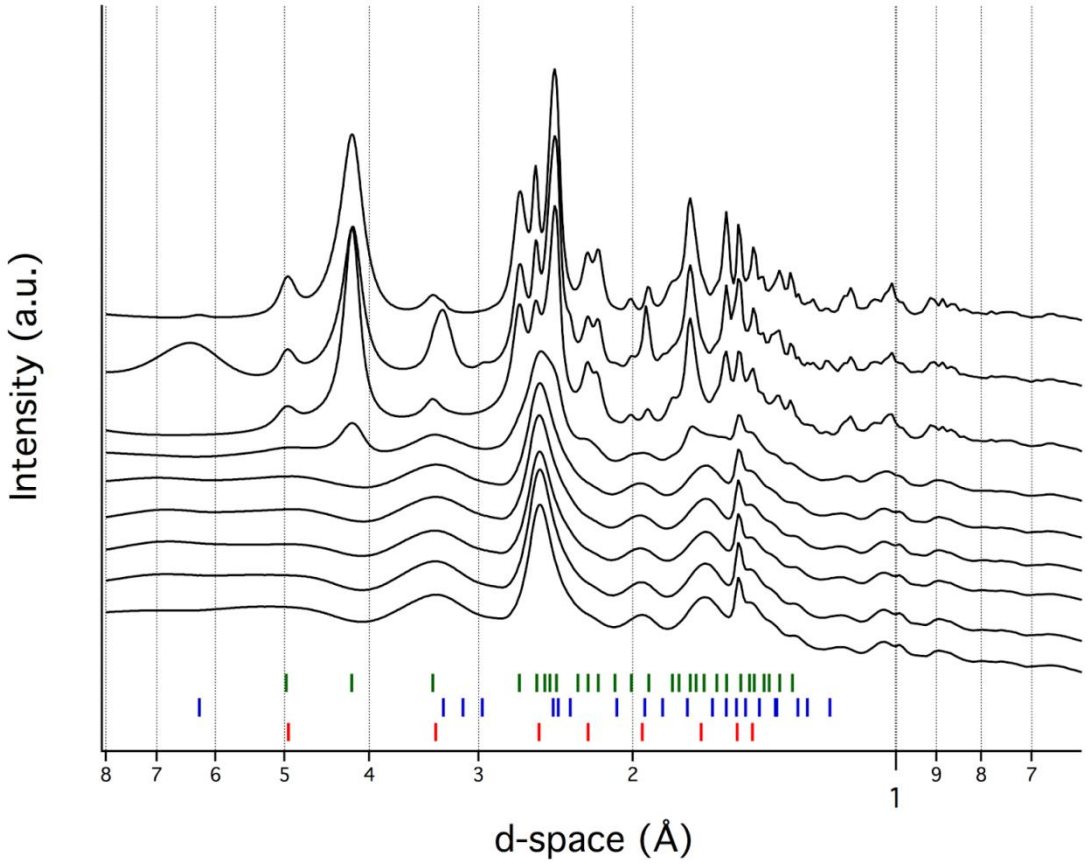

Figure B.2. Background-subtracted synchrotron powder diffraction data with intensity plotted in arbitrary units on the ordinate versus d-space in Å on the abscissa. The samples were synthesized at $[SO_4]/[Fe]=3.0$. pH increases from the bottom to the top. Lower tick marks show the calculated positions of reflections for schwertmannite (bottom, red), lepidocrocite (middle, blue) and goethite (top,green).

APPENDIX C- SUPPLEMENTARY INFORMATION

Table C.1- ICP-MS data for synthetic samples and natural samples from data reported by Caraballo et al (2013) for the S (mmol/g) and Fe/S molar ratio.

Sample ID	S (mmol/g)	Fe/S	Sample ID	S(mmol/g)	Fe/S
R1(S1)	1.44	4.62	Caraballo	1.54	5.20
R1(S2)	1.68	4.43	Caraballo	1.78	4.10
R1(S3)	1.62	4.45	Caraballo	1.37	4.70
R1(S4)	2.41	4.43	Caraballo	1.59	4.80
R1(S5)	2.69	4.67	Caraballo	1.51	5.40
R1(S6)	1.96	4.95	Caraballo	1.54	5.00
R1(S7)	0.15	8.86	Caraballo	1.59	4.90
R1(S8)	0.05	25.87	Caraballo	1.54	5.10
R1(S9)	0.05	33.94	Caraballo	1.37	5.80
R2(S1)	1.63	4.64	Caraballo	0.66	9.70
R2(S2)	1.81	4.51	Caraballo	1.12	7.30
R2(S3)	1.87	4.50	Caraballo	0.40	15.5
R2(S4)	1.68	4.39	Caraballo	0.86	8.00
R2(S5)	1.74	4.63	Caraballo	1.56	4.40
R2(S6)	1.50	5.21	Caraballo	1.60	4.70
R2(S7)	0.34	9.78	Caraballo	1.84	4.60
R2(S8)	0.12	26.11	Caraballo	1.72	4.30
R2(S9)	0.07	35.45	Caraballo	1.75	4.20
R3(S1)	2.08	4.76	Caraballo	1.60	5.40
R3(S2)	1.86	4.54	Caraballo	1.19	4.90
R3(S3)	1.74	4.48	Caraballo	1.09	5.50
R3(S4)	1.74	4.45	Caraballo	1.18	5.70
R3(S5)	2.03	4.47	Caraballo	0.53	9.60
R3(S6)	1.61	4.98	Caraballo	0.97	6.80
R3(S7)	0.34	8.55	Caraballo	0.37	11.9
R3(S8)	0.11	18.54	Caraballo	0.41	13.4
R3(S9)	0.08	32.06	Caraballo	0.38	14.7
R5(S1)	1.60	4.68	Caraballo	0.64	9.50
R5(S2)	1.66	4.57	Caraballo	0.68	9.30
R5(S3)	2.12	4.54	Caraballo	0.98	5.50
R5(S4)	1.64	4.35	Caraballo	0.49	8.80
R5(S5)	1.72	4.37	Caraballo	0.40	11.6
R5(S6)	1.47	4.97	Caraballo	1.50	4.70
R5(S7)	0.38	10.30	Caraballo	1.04	6.60
R5(S8)	0.44	16.55	Caraballo	1.59	4.8
R5(S9)	0.08	35.94	Caraballo	1.50	4.30
Caraballo	0.52	10.7	Caraballo	1.84	4.10
Caraballo	0.75	7.10	Caraballo	1.92	3.80
Caraballo	0.65	8.20	Caraballo	1.03	7.10
Caraballo	1.63	4.30	Caraballo	1.16	5.80
Caraballo	0.32	13.9	Caraballo	0.73	6.40